①

DTIC FILE COPY

AD-A230 220

CHARACTERIZATION OF MECHANICAL DAMAGE MECHANISMS IN CERAMIC AND POLYMERIC MATRIX COMPOSITE MATERIALS

By
James Lankford, Jr.
Herve Couque

TECHNICAL REPORT
ONR CONTRACT No. N00014-84-C-0213
ONR Contract Authority NR 032-553
SwRI-8124

For
Office of Naval Research
Arlington, VA 22217
By
Southwest Research Institute
San Antonio, Texas

October 1990

DTIC
S ELECTE D
DEC 14 1990
E

Reproduction in whole or in part is permitted for any purpose of the United States Government

DISTRIBUTION STATEMENT A
Approved for public release;
Distribution Unlimited

SRI
SOUTHWEST RESEARCH INSTITUTE
SAN ANTONIO HOUSTON DETROIT
WASHINGTON, DC DALLAS/FT. WORTH

UNCLASSIFIED

SECURITY CLASSIFICATION OF THIS PAGE

REPORT DOCUMENTATION PAGE

Form Approved
OMB No. 0704-0188
Exp.Date: Jun 30, 1986

1a. REPORT SECURITY CLASSIFICATION
Unclassified

1b. RESTRICTIVE MARKINGS

2a. SECURITY CLASSIFICATION AUTHORITY

2b. DECLASSIFICATION/DOWNGRADING SCHEDULE

3. DISTRIBUTION/AVAILABILITY OF REPORT
~~Distribution Limited~~

4. PERFORMING ORGANIZATION REPORT NUMBER(S)
06-8124

5. MONITORING ORGANIZATION REPORT NUMBER(S)
NR 032-553

6a. NAME OF PERFORMING ORGANIZATION
Southwest Research Institute

6b. OFFICE SYMBOL *(If applicable)*

7a. NAME OF MONITORING ORGANIZATION
Dr. Steven G. Fishman - Code 431N
Office of Naval Research

6c. ADDRESS *(City, State, and ZIP)*
6220 Culebra Road, PO Drawer 28510
San Antonio, TX 78228-0510

7b. ADDRESS *(City, State, and ZIP Code)*
800 North Quincy Street
Arlington, VA 22217

8a. NAME OF FUNDING/SPONSORING ORGANIZATION
Office of Naval Research

8b. OFFICE SYMBOL *(If applicable)*

9. PROCUREMENT INSTRUMENT IDENTIFICATION NUMBER
N00014-84-C-0123

8c. ADDRESS *(City, State, and ZIP)*
800 North Quincy Street
Arlington, VA 22217

10. SOURCE OF FUNDING NUMBERS

PROGRAM ELEMENT NO.	PROJECT NO.	TASK NO.	WORK UNIT ACCESSION NO.

11. TITLE *(Include Security Classification)*
Characterization of Mechanical Damage Mechanisms in Ceramic Composite Materials

12. PERSONAL AUTHOR(S)
James Lankford and Herve Couque

13a. TYPE OF REPORT
Technical

13.b TIME COVERED
FROM 10/89 TO 10/90

14. DATE OF REPORT *(Year, Month, Day)*
October 1990

15. PAGE COUNT
59

16. SUPPLEMENTARY NOTATION

17. COSATI CODES

FIELD	GROUP	SUB-GROUP

18. SUBJECT TERMS *(Continue on reverse if necessary and identify by block number)*
Key Words: compressive strength, whisker-reinforced, composite materials; fracture mechanisms; ceramics; plastic flow ; ceramic matrix fiber reinforcement.

19. ABSTRACT *(Continue on reverse if necessary and identify by block number)*

The principal objective of the program has been to establish the loading rate dependence of compressive deformation and fracture mechanisms in whisker and fiber-reinforced ceramic matrix composites, and in fiber-reinforced polymeric matrix composites. Work during the last year has emphasized several types of composite: SiC fiber and SiC whisker-reinforced pyroceram, and graphite fiber-reinforced thermoplastic.

The behavior of a unidirectional carbon fiber-reinforced thermoplastic matrix composite subject to compressive loading at strain rates ranging from 10^{-5} sec^{-1} to 5000 sec^{-1} is reported. Damage mechanisms are identified, and discussed in terms of matrix microstructure and fiber interactions. In particular, it is found that under quasi-static conditions, two absolutely critical factors control the life of the composite, i.e., the ability of the polymeric matrix to resist shear and thereby inhibit fiber flexure, and the ability of individual fibers to resist the nucleation of compressive plastic shear bands during flexure. It also is shown that at very high rates of strain (~ 5000s^{-1}), the strength suddenly begins to increase with strain rate in an extremely robust fashion. The measured strength-strain rate dependence in this range is shown to be consistent with the kinetics of kink band propagation.

(Continued)

20. DISTRIBUTION/AVAILABILITY OF ABSTRACT
☒ UNCLASSIFIED/UNLIMITED ☐ SAME AS RPT. ☐ DTIC USERS

21. ABSTRACT SECURITY CLASSIFICATION
Unclassified

22a. NAME OF RESONSIBLE INDIVIDUAL
James Lankford

22b. TELEPHONE *(Include Area Code)*
512/522-2317

22c. OFFICE SYMBOL

DD FORM 1473 84 MAR

83 APR edition may be used until exhausted.
All other editions are obsolete.

SECURITY CLASSIFICATION OF THIS PAGE

UNCLASSIFIED

19. ABSTRACT (Continued)

The compressive strength of pyroceramic reinforced with a wide variety of SiC whiskers is characterized at loading rates which range from quasi-static to dynamic. It is found that strength is inversely related to whisker size, and essentially strain rate insensitive. The same strain rate independence is obtained for unreinforced matrix, but the strength of the latter lies below that for small (≤ 1 μm diameter) whisker-reinforced composites, and above that for large (> 3 μm diameter) whisker material. Whisker/crack interaction and (to a lesser extent) whisker pullout seem to be responsible for the beneficial small whiskers, while the apparently detrimental large whiskers serve as microcrack-nucleating inclusions.

The tensile strength and associated failure micromechanisms have been characterized for a SiC fiber-reinforced ceramic matrix composite subject to strain rates in excess of $1000 s^{-1}$. It is found that behavior under such conditions is not described by the current matrix fracture/fiber pullout models. This is a consequence of the rapid and extreme frictional heating produced at the fiber-matrix interface by sliding velocities as high as 1000 m/s. At sufficiently rapid loading rates, the near-interface matrix appears to virtually melt, and the frictional interface shear resistance is reduced to the point that the fibers debond throughout the specimen, and pull out without failing. This suggests that for sufficiently rapid loading, the stress to fail the specimen will approach that merely to cause the initial matrix crack, i.e., a stress level well below the ultimate strength normally attainable under quasi-static conditions.

Accession For
NTIS GRA&I ☒
DTIC TAB ☐
Unannounced ☐
Justification

By
Distribution/
Availability Codes

Dist	Avail and/or Special
A-1	

Statement "A"; RDP title should read same as cover per telecon Dr. Steven Fishman. Office of Naval Research/code 1131.

VHG 12/14/90

COPY INSPECTED

FOREWORD

This report describes recent work carried out under an experimental program aimed at characterizing damage mechanisms and compressive failure in ceramic and polymeric matrix composite materials. The report consists of three papers, each having been submitted for publication as noted on its title page.

TABLE OF CONTENTS

Page

I. COMPRESSIVE DAMAGE AND FAILURE AT HIGH LOADING RATES IN GRAPHITE FIBER-REINFORCED POLYMERIC MATRIX COMPOSITES 1

II. INFLUENCE OF MICROSTRUCTURE AND STRAIN RATE ON THE COMPRESSIVE STRENGTH OF WHISKER-REINFORCED CERAMIC MATRIX COMPOSITES 17

III. EFFECT OF DYNAMIC LOADING ON TENSILE STRENGTH AND FAILURE MECHANISMS IN A SIC FIBER-REINFORCED CERAMIC MATRIX COMPOSITE 37

Proceedings of the Second International Conference on Composites (in press)

I.

COMPRESSIVE DAMAGE AND FAILURE AT HIGH LOADING RATES IN GRAPHITE FIBER-REINFORCED POLYMERIC MATRIX COMPOSITES

James Lankford
Southwest Research Institute
P. O. Drawer 28510
San Antonio, Texas 78228-0510

ABSTRACT

The behavior of a unidirectional carbon fiber-reinforced thermoplastic matrix composite subject to compressive loading at strain rates ranging from 10^{-5}sec^{-1} to $5000\ \text{sec}^{-1}$ is reported. Damage mechanisms are identified, and discussed in terms of matrix microstructure and fiber interactions. In particular, it is found that under quasi-static conditions, two absolutely critical factors control the life of the composite, i.e., the ability of the polymeric matrix to resist shear and thereby inhibit fiber flexure, and the ability of individual fibers to resist the nucleation of compressive plastic shear bands during flexure. It also is shown that at very high rates of strain (~ 5000s^{-1}), the strength suddenly begins to increase with strain rate in an extremely robust fashion. The measured strength-strain rate dependence in this range is shown to be consistent with the kinetics of kink band propagation.

I. INTRODUCTION

While there has been considerable effort to understand the mechanism of compressive failure in polymeric-matrix composites,[1-3] most of this work has involved the study of gross features such as macroscopic shear bands and longitudinal splitting. Unfortunately, this sort of information does not provide a basis for predicting the onset of the initial instability, and since failure following initiation is such a rapid process, it is the early damage events which are most critical. In addition, recent work[4] on the compressive failure of unreinforced individual fibers suggests that this initiation phase, and the propagation of a resulting kink band, may be much more complex than previously appreciated.

Moreover, certain practical situations require that fiber-reinforced polymeric matrix composites be able to withstand impulsive compressive loadings parallel to the fiber direction. To date, the strengths of thermoset (epoxy) matrix composites have been investigated under variable strain rate conditions,[5,6] but only recently[7] has such study been devoted to the fairly new carbon fiber-thermoplastic resin class of material. The objective of the present paper is to report on the characterization of strength and damage mechanisms for one of these composites subject to compressive loading at strain rates ranging from quasi-static to greater than 1000 s^{-1}.

In order to achieve such rates of deformation, it is necessary to use special mechanical test techniques, in this case the split Hopkinson pressure bar (SHPB). However, the axially-symmetric geometry of this machine precludes utilization of the special gripping arrangements devised[1,8] to defeat the geometric problems which plague accurate assessment of the compressive strength of composites. A subsidiary effort was therefore undertaken to develop a test specimen which would permit relatively smooth elastic wave propagation within the SHPB-specimen system, while at the same time generating reliable strength data based on intrinsic compressive failure mechanisms.

II. EXPERIMENTAL PROCEDURES

Materials

The material selected for study was a polyetheretherketone (PEEK) matrix, polyacrylonitrile (PAN)-derived carbon fiber-reinforced composite.* The matrix is a semicrystalline thermoplastic of approximately 23000 molecular weight, whose properties and microstructure are extremely sensitive to thermal history.[9] In producing the present composite, the matrix was melt impregnated at 380°C for 30 minutes; subsequent heat treatment resulted in a spherulitic microstructure, revealed by argon ion etching, on the order of 8 μm in size.

---

* Aromatic Polymer Composite Two (APC-2), ICI Ltd.

Approximately 7 μm diameter AS4 carbon fibers were laid up unidirectionally, with a nominally 60% fiber density. There was a significant waviness to the fibers, i.e., uniaxial alignment was by no means perfect, and although the void density was under 1%, the voids which were present tended to cluster. Both of these defects are typical of PEEK/carbon fiber composites.

Establishment of Specimen Configuration

Compression testing of polymeric matrix/graphite fiber-reinforced composites has been reviewed by Adsit[8] and, more recently, by Lee.[1] Most of the reliable test techniques require a flat panel specimen geometry, and several have been judged compatible with ASTM requirements. To date, the highest quasi-static compressive strength for the particular composite material employed in the present study has been obtained[1] by means of the so-called Celanese gripping arrangement, which involves a conical-shaped wedge fixture. Thus, the requirement in the present instance was to produce, using an end-loaded axially-symmetric specimen, a compressive strength on the order of that achieved using the more elaborate Celanese technique, and (just as important) failure within the specimen gage section, unassociated with gripping or end effects.

Several specimen designs were evaluated in the sequence (A-E) shown in Figure 1. The internally chamfered rings around the bases of specimens B-E were made of high strength steel, honed to a snug fit. All specimens, as well as matching hardened steel load platens, were carefully machined so that the mating surfaces were parallel within 4 μm over the load surface diameter. Quasi-static compression tests were performed at a strain rate of $1.6 \times 10^{-4} s^{-1}$ under crosshead control in a servo-controlled hydraulic machine. Acoustic emission (AE) was monitored by means of a transducer resonant at 160 kHz, filtered below 100 kHz and above 1 GHz.

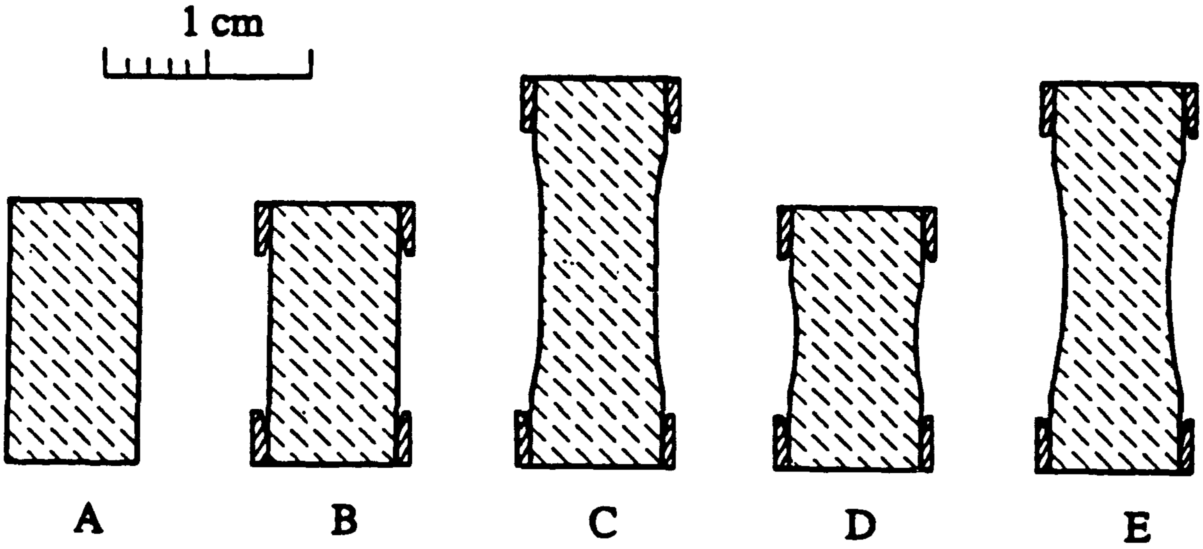

Figure 1. Cross-sectional views of candidate compression specimens.

Average strengths (σ_c) for several tests of each specimen design (with the exception of design A) are given in Table 1, together with results obtained by Lee[1] using the Celanese configuration for two different batches of material, each nominally identical to the present composite. Specimens configured in design A failed at a low stress by brooming, which initiated early in the test as evidenced by the AE. Type B and C specimens were stronger, but sectioning and polishing showed that each failed by means of shear bands nucleated at the stress concentrations imposed by the anti-brooming rings. Types D and E were considered to be successful; strength levels were compatible with the Celanese design, and failure occurred via shear bands located near the center of the gage section. The essentially equivalent strength results for the latter designs (compare with the range in the Celanese specimen tests,[1] Table 1) suggested that the smaller reduced section radius of type D was not a liability, and this was selected as the standard specimen for subsequent experiments. It should be noted that the angle of the shear bands with the load axis (Table 1) was virtually constant for all four ringed designs, and that the AE results indicated that the bands probably initiated just prior to failure.

Table 1.
Comparative Compressive Behavior for Candidate Specimen Configurations

Configuration	σ_c (MPa)	Shear Band Angle (°)
A	823	(brooming)
B	985	75
C	1288	76.0
D	1330	75.5
E	1389	73.0
Celanese (Ref. 1)	1316;1409	75

Higher Strain Rate Experiments

In addition to the quasi-static tests, it was possible to attain strain rates ($\dot{\varepsilon}$) on the order of 1 s^{-1} by means of the hydraulic machine. However, a still higher strain rate regime, $\dot{\varepsilon} = 500 - 5000 s^{-1}$, can be attained by utilizing the split Hopkinson pressure bar apparatus. The details of the technique have been described elsewhere;[10] however, for present purposes it should be noted that this involves the creation within the specimen of a rapidly rising impulsive load generated by means of a projectile fired against one of two steel rod wave guides which sandwich the specimen. For non-ductile materials, the strain rate is computed as the slope of the leading edge of this pulse (the stress rate) divided by the elastic modulus of the composite. Unfortunately, under such circumstances, a relatively brittle specimen tends to fail catastrophically at a critical stress level, so that efforts to save it, for example by means of a strain-limiting insert, usually are futile. In the present instance, then, efforts to understand failure micromechanisms necessarily will be confined to quasi-static experiments. However, the case will be made that in this particular instance, those mechanisms in modified form, probably are responsible for the SHPB results as well.

Damage Characterization Experiments

In order to understand the microstructural basis for the compressive behavior of the specimens, several of them were sectioned and examined by optical and scanning electron microscopy (SEM). It was found necessary, in order to capture shear bands in the desired early stages of development, to slow the quasi-static tests even further just prior to failure, i.e., to a strain rate of approximately $10^{-6}s^{-1}$. By this means, it was possible to detect the surface relief change just as kink bands nucleated.

Some of the sections were examined in the as-polished state. However, it also was found useful to subject certain samples to nitrogen ion beam milling, which revealed additional deformation features. For SEM study, specimens were vapor-deposited with gold.

III. RESULTS

A typical quasi-static stress-strain (σ-ε) curve is shown in Figure 2. As indicated, the relationship deviates from linearity well before failure, which is virtually instantaneous. Acoustic emission is not associated with yielding, but does occur just prior to failure. Similar deformation behavior is obtained for strain rates as high as 2 s^{-1}. However, such relatively subtle yielding, corresponding to a total plastic strain at failure on the order of 0.0015, cannot be discriminated in the SHPB results, and valid AE data cannot be obtained for such brief experiments.

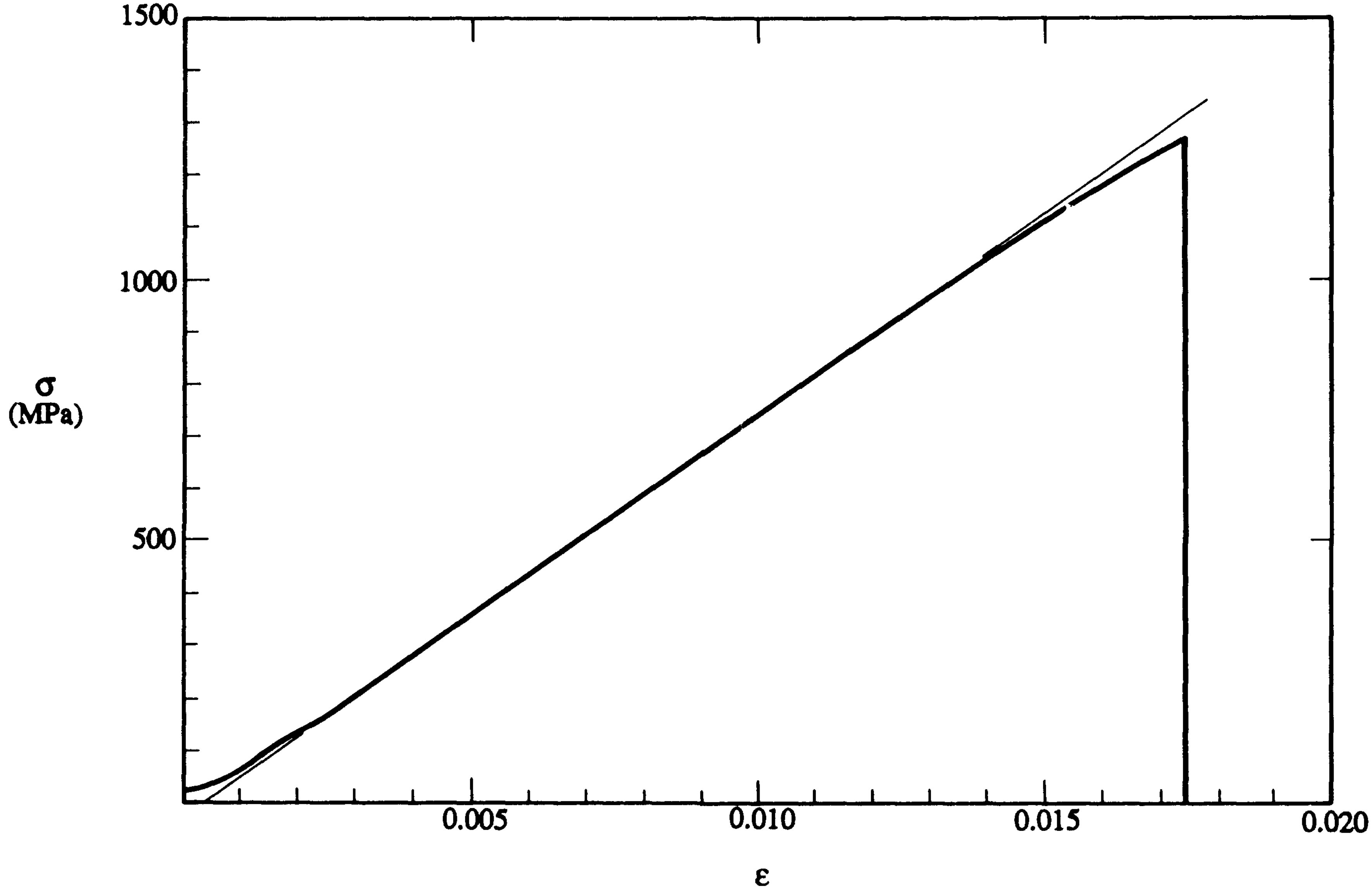

FIGURE 2. Compressive stress-strain response, $\dot{\varepsilon} = 1.6 \times 10^{-4} s^{-1}$.

Results are summarized in Figure 3, in terms of compressive strength (σ_c), yield strength (σ_y, defined as onset of departure from the initial load line), and strain rate ($\dot{\varepsilon}$). Stress levels for the onset of AE are not plotted, as they are so near in value to σ_c. It is evident that for $\dot{\varepsilon} \lesssim 1000 s^{-1}$, both σ_c and σ_y increase only very gradually with strain rate, while for $\dot{\varepsilon} \gtrsim 3000 s^{-1}$, the dependence is much more robust, with $\sigma_c \propto \dot{\varepsilon}^{0.92}$.

As shown in Figure 4, failed specimens are characterized by the presence of a kink band oriented at approximately 7° to the load axis. Such a band in the process of development is shown in Figure 5. It is evident [Figure 6(a)] that the two boundaries of such kinks are composed of broken fibers, while the matrix is unfractured. On the other hand, the matrix must be deformed significantly as indicated [Figure 6(b)] by the altered fiber spacing (d) within the kink versus the initial value (d_0). The fibers have fractured on the tensile side of the kink; without fracturing the matrix, the resulting microcracks have opened as though rotating about a point on the opposite (compressive) side of each fiber.

This apparent rotation is accommodated as shown in Figure 7(a), in which ion etching has revealed the presence of several shear deformation bands on the compressive side of the fiber. Also within the field of view is the tip of a microcrack approaching from the tensile side of the fiber. By tilting the page and peering along the edge of the fiber, it can be seen that the latter is curved continuously within this sector, a curve which is composed of the almost straight fiber segments between, and adjacent to, the shear bands.

The final step in the kink failure process is shown in Figure 7(b). Here the microcrack approaching from the right has deviated radically from its flexure-driven path, and linked-up with deformation band 1. By again tilting the page, it appears that the other two bands (arrows) have relaxed, and are almost parallel to the original edges of the fiber. The local kink now rotates about a single point: the origin of band 1, where the crack tip resides.

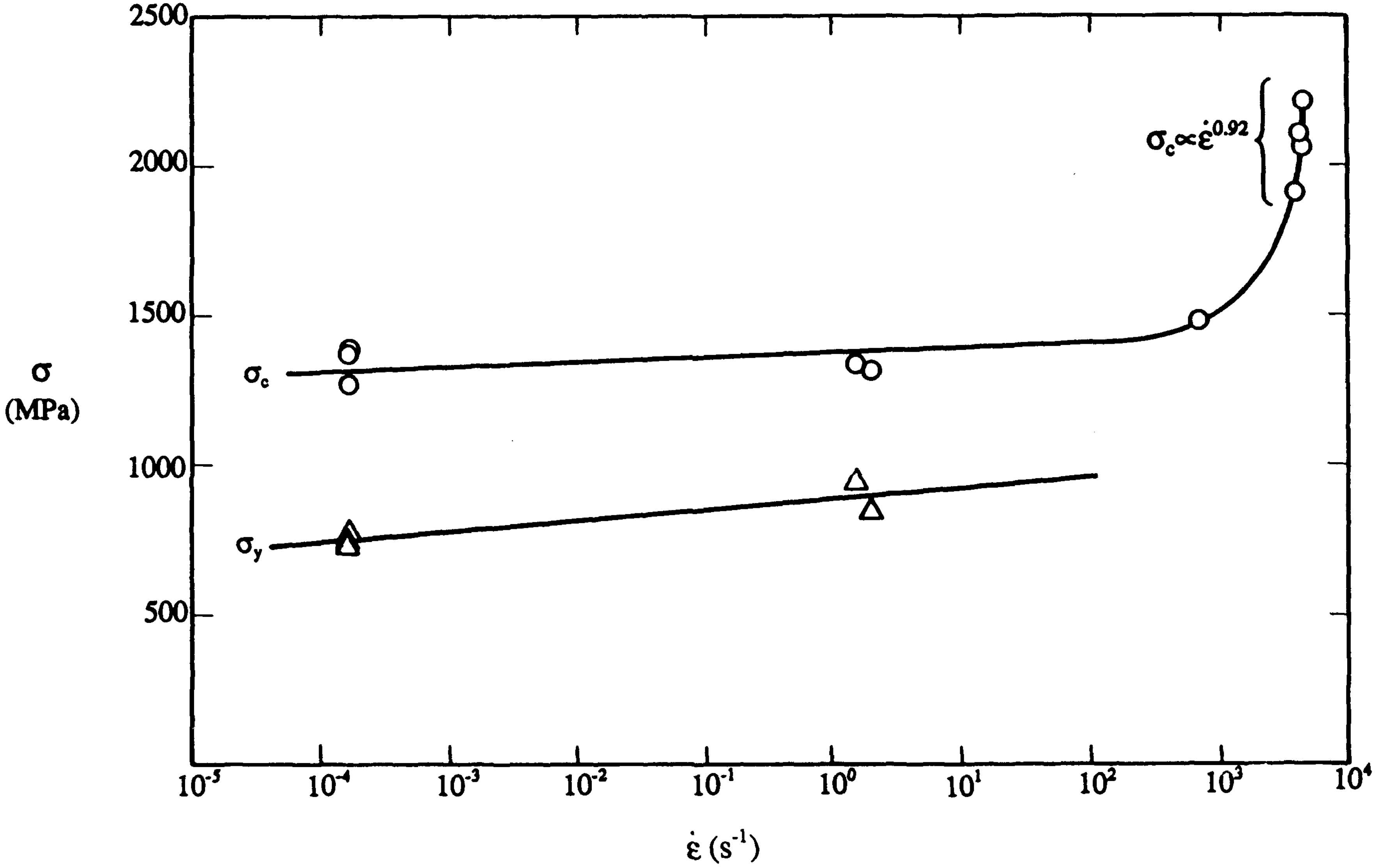

Figure 3. Strength versus strain rate.

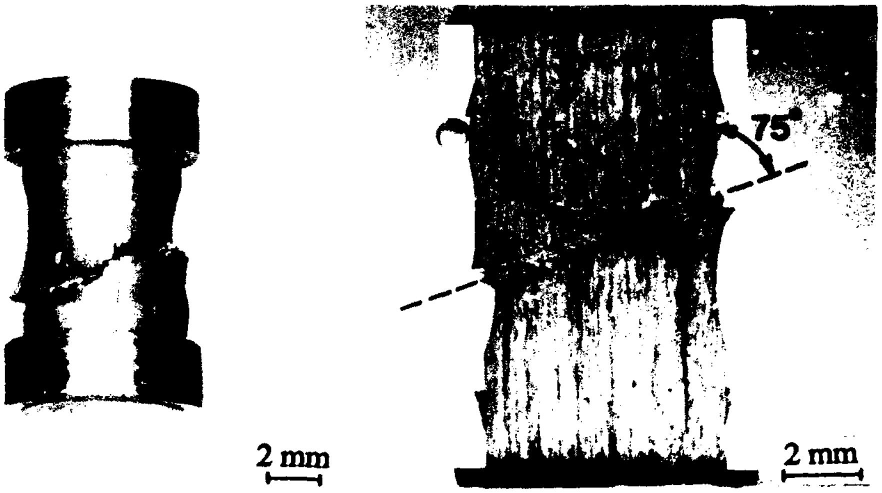

(a) Shear failure.

(b) Polished section showing orientation of shear band.

FIGURE 4 Failed specimen, $\dot{\varepsilon} = 1.6 \times 10^{-4} s^{-1}$.

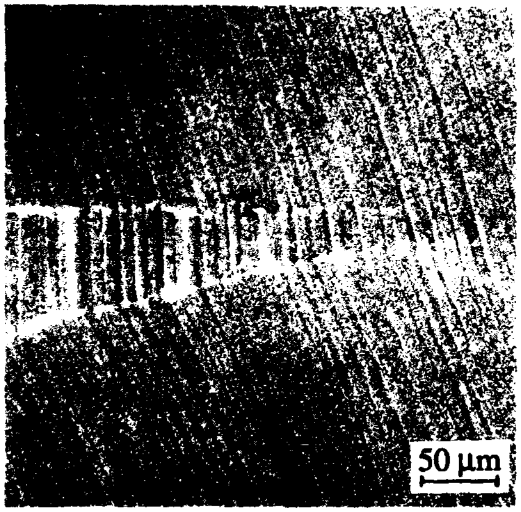

FIGURE 5 macroscopic view of arrested kink band.

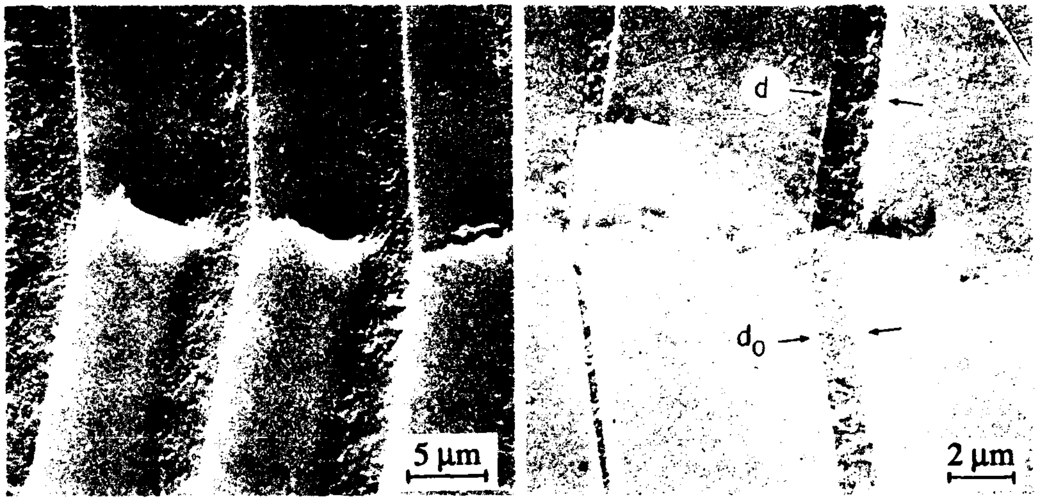

(a) Upper edge of kink band, showing fiber fracture matrix and fiber-matrix interface intact.

(b) Lower edge of kink band showing tensile extension of matrix material normal to fibers within band.

FIGURE 6 Fiber matrix response within kink band; ion milled surface.

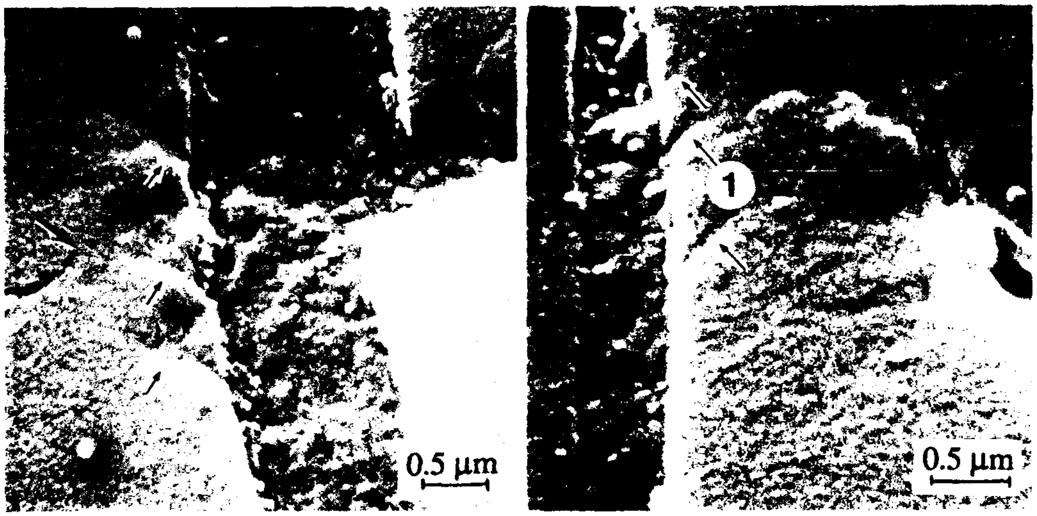

(a) Multiple compressive deformation bands (small arrows); arrested crack tip (large arrow).

(b) Last stage of fiber failure: crack path alteration by presence of deformation band 1; other bands (arrows) relaxed. Note shear offsets at fiber-matrix interface.

FIGURE 7 Details of fiber kinking, ion milled surface.

IV. DISCUSSION

The following discussion consists of two parts. In the first, the basic compressive failure process is considered, while in the concluding section, the implications of this mechanism for dynamic failure are hypothesized.

Compressive Failure

Based on the foregoing results, it is clear that the compressive failure of PAN-carbon fiber-reinforced PEEK is a complex process. The sequence of events appears to obey the following scenario, some aspects of which derive from the ideas of Evans and Adler[11] pertaining to kinking in carbon fiber composites.

At moderate loading rates, the composite yields well before failure, with no AE or otherwise detectable (optical or SEM) microstructural damage. However, this slight yielding is eventually responsible for permitting preferentially aligned (or located, relative to voids) individual fibers to flex or buckle, and approach the condition for fiber fracture. The absence of constraint near a free surface dictates that the latter generally will be the site of kink nucleation. At this time, and this time alone in the kinking process, the flaw probability statistics of fiber fracture come into play.[11] Once a few adjacent fibers whose critical flaws happen to lie near the future macroscopic kink plane fail, the subsequent propagation of the kink is controlled by the deformation field at its tip.

The kink band grows by slightly flexing fibers in its path, and then failing them in compression. In a recent series of elegant "recoil" compression experiments, Dobb, et al.,[4] have shown that individual PAN-based fibers fail by first forming deformation bands on their inner compressive sides as they buckle slightly. The criterion for nucleating these bands is based on the intrinsic strength of a typical fiber. In effect, the deformation bands constitute "microkinks," which localize fiber flexure, and cause the nucleation of tensile microcracks on the opposite side of the fiber. It is observed that flaws are not present at the origins of these microcracks, and that fiber fracture is accomplished by the linkup of the tensile microcrack with one of the compressive deformation bands. The latter generally requires the crack to deviate from its nominal fracture plane.

This appears to be precisely what happens to flexed fibers at the tip of a propagating macroscopic kink in the composite. As shown in Figure 7(a), multiple deformation bands are present on the compressive side of a fiber prior to the time the tensile crack tip arrives, and fiber fracture is completed by linkup of the microcrack with one of the deformation bands. Because of the energy stored within the deformed matrix, fiber fracture permits this local system to relax, and the fiber microkink bands are reversed [Figure 7(b)]. This is understandable, since the interfiber tensile strains are quite high. From Figure 6(b), for example, an estimate of this strain is given by $(d - d_0) / d_0$, or 0.33. It is perfectly reasonable that such intense local tensile deformation occurs; tensile fracture experiments by Saiello, et al.,[12] show that the strength of the fiber matrix interface (for semi-crystalline matrices) exceeds that of the matrix, and interlaminar fracture studies[13] indicate that large interfiber tensile strains are generated prior to failure.

Strain Rate Effects

Clearly, increasing the strain rate will inhibit the thermally activated molecular processes responsible for matrix deformation, and this must be responsible for the gradual increase in σ_y with $\dot{\varepsilon}$ at low to intermediate strain rates. The fact that σ_c increases similarly over the same range apparently reflects the role of matrix constraint in the individual (or small cluster) fiber buckling which precedes the nucleation of fiber deformation bands. As the yield strength increases, it becomes more difficult for fibers to buckle, thus raising σ_c proportionately. These observations support the contention developed above that under moderate rates of loading, it is kink nucleation, accompanied by matrix flow, which is the key event at failure; subsequent kink band propagation is inevitable, and essentially instantaneous. On the other hand, the situation appears to be reversed at rapid strain rates.

It is not absolutely certain that kinking remains the dominant mode of failure for strain rates in excess of $1000 s^{-1}$, as the specimens are largely destroyed in the experiment. But in the absence of evidence to the contrary, it seems highly likely that this should be so. This has, in fact, been found[14] to be the case for a SiC-reinforced pyroceramic-matrix composite, whose post-failure deformation was sufficient that SHPB tests could be stopped prior to complete disintegration of the specimen. In that work, the kinetics of failure by kink propagation were considered, and it was shown that at high loading rates (i.e., high enough that the time required for failure is on the order of that needed for the trans-specimen passage of a wave moving at the sound speed), the strength should be directly proportional to the strain rate, i.e., $\sigma_c \propto \dot{\varepsilon}^{1.0}$. The results plotted in Figure 3 for $\dot{\varepsilon} \gtrsim 3000\text{s}^{-1}$ obey a relationship ($\sigma_c \propto \dot{\varepsilon}^{0.92}$) which certainly is compatible with this theory, although the available strain rate range is so narrow that the data cannot be said to prove the point absolutely.

At such high deformation rates, it is highly likely that thermally activated matrix deformation is prohibited. In that case, fiber kink nucleation and propagation will be accommodated by matrix microfracture, rather than plastic flow. This will not alter the underlying high strain rate σ_c - $\dot{\varepsilon}$ proportionality, however, since kink velocity is the controlling factor, and the latter is primarily a function of the sound speed. That is, thermally activated deformation processes, and even matrix microfracture, for which σ_c is frequently found[15] to be proportional to $\dot{\varepsilon}^{0.33}$, simply are much less robust functions than that which controls kink propagation. Hence, it will little matter if there should be a transition in the mechanism by which the matrix accommodates the passage of a kink band.

V. ACKNOWLEDGEMENTS

The careful and skillful experimental work of, and helpful discussions with, A. Nicholls and J. Campbell are acknowledged with appreciation. Support of the Office of Naval Research through contract No. N00014-84-C-0213 is gratefully acknowledged.

VI. REFERENCES

1. R. J. Lee, "Compression Strength of Aligned Carbon Fiber-Reinforced Thermoplastic Laminates," *Composites*, **18** (1), 35-39, 1987.

2. D. Purslow, "Fractography of Fiber-Reinforced Thermoplastics, Part 3. Tensile, Compressive, and Flexural Failures," *Composites*, **19** (5), 358-366,1988.

3. E. G. Guynn and W. L. Bradley, "A Detailed Investigation of the Micromechanisms of Compressive Failure in Open Hole Composite Laminates," *J. Comp. Mats.*, **23** (5), 479-504, 1989.

4. M. G. Dobb, D. J. Johnson, and C. R. Park, "Compressional Behavior of Carbon Fibers," *J. Mat. Sci.*, **25** (2), 829-834, 1990.

5. C. Cazeneuve and J. -C. Maile, "Study of the Behavior of Carbon Fiber-Reinforced Composites at Different Rates of Deformation," *J. Physique*, **46** (8), 551-556, 1985.

6. P. Kumar, A. Garg, and B. D. Agarwal, "High Strain Rate Behavior of Unidirectional GFRP," *J. Aero. Soc. India*, **38** (1), 11-16, 1986.

7. D. M. Montiel and C. J. Williams, "A Method for Evaluating the High Strain Rate Compressive Properties of Composite Materials," *Composite Materials: Testing and Design*, ASTM STP (in press).

8. N. R. Adsit, "Compression Testing of Graphite/Epoxy," *Compression Testing of Homogeneous Materials and Composites," ASTM STP 808*, ed. R. Chait and R. Papirno, American Society for Testing and Materials, Philadelphia, 175-186.1983.

9. J. -N. Chu and J. M. Schultz, "The Influence of Microstructure on the Failure Behavior of PEEK," *J. Mat. Sci.*, **24** (12), 4538-4544,1989.

10. U. S. Lindholm and L. M. Yeakley, "High Strain Rate Testing: Tension and Compression," *Exp. Mech.*, **8** (1), 1-9, 1968.

11. A. G. Evans and W. F. Adler, "Kinking as a Mode of Structural Degradation in Carbon Fiber Composites," *Acta Met.*, **26** (5), 725-738, 1978.

12. S. Saiello, J. Kenny, and L. Nicolais, "Interface Morphology of Carbon Fiber/PEEK Composites," *J. Mat. Sci.*, **25** (9), 3493-3496, 1990.

13. S. Hashemi, A. J. Kinloch, and J. G. Williams, "The Effects of Geometry, Rate, and Temperature on the Mode I, Mod II, and Mixed-Mode I/II Interlaminar Fracture of Carbon-Fiber/Poly(ether-ether ketone) Composites," *J. Comp. Mats.*, **24** (9), 918-956, 1990.

14. J. Lankford, "Dynamic Compressive Fracture in Fiber-Reinforced Ceramic Matrix Composites," *Mats. Sci. Eng.*, **A107** (1) 261268, 1989.

15. J. Lankford, "The Role of Subcritical Tensile Microfracture Processes," *Fracture Mechanics of Ceramics*, Vol. 5, ed. R. C. Bradt, A. G. Evans, D. P. H. Hasselman, and F. F. Lange, Plenum Press, New York, 625-637, 1983.

Submitted to Journal of Materials Science

II.

INFLUENCE OF MICROSTRUCTURE AND STRAIN RATE ON THE COMPRESSIVE STRENGTH OF WHISKER-REINFORCED CERAMIC MATRIX COMPOSITES

James Lankford
Southwest Research Institute
P. O. Drawer 28510
San Antonio, Texas 78228-0510

ABSTRACT

The compressive strength of pyroceramic reinforced with a wide variety of SiC whiskers is characterized at loading rates which range from quasi-static to dynamic. It is found that strength is inversely related to whisker size, and essentially strain rate insensitive. The same strain rate independence is obtained for unreinforced matrix, but the strength of the latter lies below that for small (≤ 1 μm diameter) whisker-reinforced composites, and above that for large ($\gtrsim 3$ μm diameter) whisker material. Whisker/crack interaction and (to a lesser extent) whisker pullout seem to be responsible for the beneficial small whiskers, while the apparently detrimental large whiskers serve as microcrack-nucleating inclusions.

I. INTRODUCTION

The strengthening/toughening of ceramic matrices by the introduction of ceramic whiskers are receiving considerable current attention.[1] However, most of this effort has been devoted to tensile or flexural loading conditions, for which a variety of fiber-matrix interactions (microcracking process zone; phase transformation-induced residual stress field; crack deflection; crack bridging/whisker pullout) have been identified.[2,3] It has been shown that these interactions are quite promising,[1] and models are being developed to guide optimization of composite architecture in terms of these mechanisms.

On the other hand, almost no consideration has been given to the performance and underlying constituent interactions of whisker-reinforced ceramics subject to compressive stresses. Since it is thought that this family of composites may be particularly useful in applications involving wear and impact,[1] it clearly is relevant to try and understand their behavior under compression over a wide range in rate of loading. Previously, the compressive strength of a SiC fiber-reinforced silicon nitride matrix had been determined under both quasi-static and dynamic (near impact) strain rates. It was found that the whiskers degraded the strength of the matrix under quasi-static conditions, but at strain rates in excess of about $1000s^{-1}$, the strength began to increase at an extremely rapid rate (i.e., relative to rising strain rate), and the composite versus matrix strength differential observed at lower rates of loading disappeared. The objective of the present study was to expand this limited base of knowledge by investigating a different class of matrix, prepared in two fundamentally different microstructural variants, reinforced with a wide variety of whisker types.

II. MATERIAL

The material chosen for study was fabricated by United Technologies Research Center (UTRC). It was prepared as described in detail by Brennan,[5] and briefly as follows. Lithium aluminosilicate powder (denoted as LAS-I by UTRC) was hot-pressed with several commercially available SiC whiskers; all composites were formulated to contain 30 vol.% whiskers. In the as-pressed state, the matrix was glassy. A drastically different microstructure was produced by heat-treating the material in argon at 900°C for 24 hours, which crystallized the material in the form of 0.5 - 2 μm grains of β-spodumene/silica solid solution phase in the β-quartz crystal structure. The dimensions of the whiskers, and the tensile mechanical properties[5] of the resultant composites and the two matrix variants (glassy and crystalline, denoted by material postscripts 1 and 2, respectively) are given in Table I. Also listed is a closely related pyroceram, Corning 9606, in the ceramed state. Although equivalent tensile strength and toughness were not known, its compressive behavior was previously characterized,[6] and will be compared with that of the present composites; unfortunately, no pure LAS-I, in either the as-pressed or ceramed condition, was available for

Table I
Material Parameters

Material	Whisker Diameter (μm)	Condition	3-Bend Flexural Strength (MPa)	Fracture Toughness (MPa - $m^{1/2}$)
A1	< 0.7*	As-Pressed	400	4.73
A2		Ceramed	393	4.44
T1	1.0**	As-Pressed	358	3.82
T2		Ceramed	373	4.06
AMI 1	3.0***	As-Pressed	166	2.83
AMI 2		Ceramed	193	2.83
LANL 1	5-8****	As-Pressed	110	2.29
LANL 2	---	Ceramed	103	2.24
LAS 1	---	As-Pressed	83	0.80
LAS 2	---	Ceramed	138	1.00
Pyroceram+	---	Ceramed	---	---

*	Arco SC-9
**	Tokai TWS-400
***	American Matrix Inc.
****	Los Alamos National Laboratory
+	Corning 9606

compression testing. However, Corning 9606 and UTRC LAS-I are sufficiently similar chemically and microstructurally that it seems highly likely that they would share equivalent compressive response.

Microstructures of the four basic composites are shown in Figure 1. In these low-magnification views, the generally heterogeneous whisker dispersion is evident; only the T2 material is relatively homogeneous. It should be emphasized that similar dispersions prevail in the as-pressed (glassy) state as well. The relative sizes and aspect ratios of the individual whiskers are shown in Figure 2. In addition to the whiskers, considerable particulate debris is included in the microstructures. Surface characterization by Brennan[5] has shown that all four of the whisker variants are covered with carbon-rich films. In addition, the Arco and LANL whiskers are very smooth; the Tokai whiskers are fairly smooth, but wavy in profile; and the AMI whiskers are very rough in surface morphology.

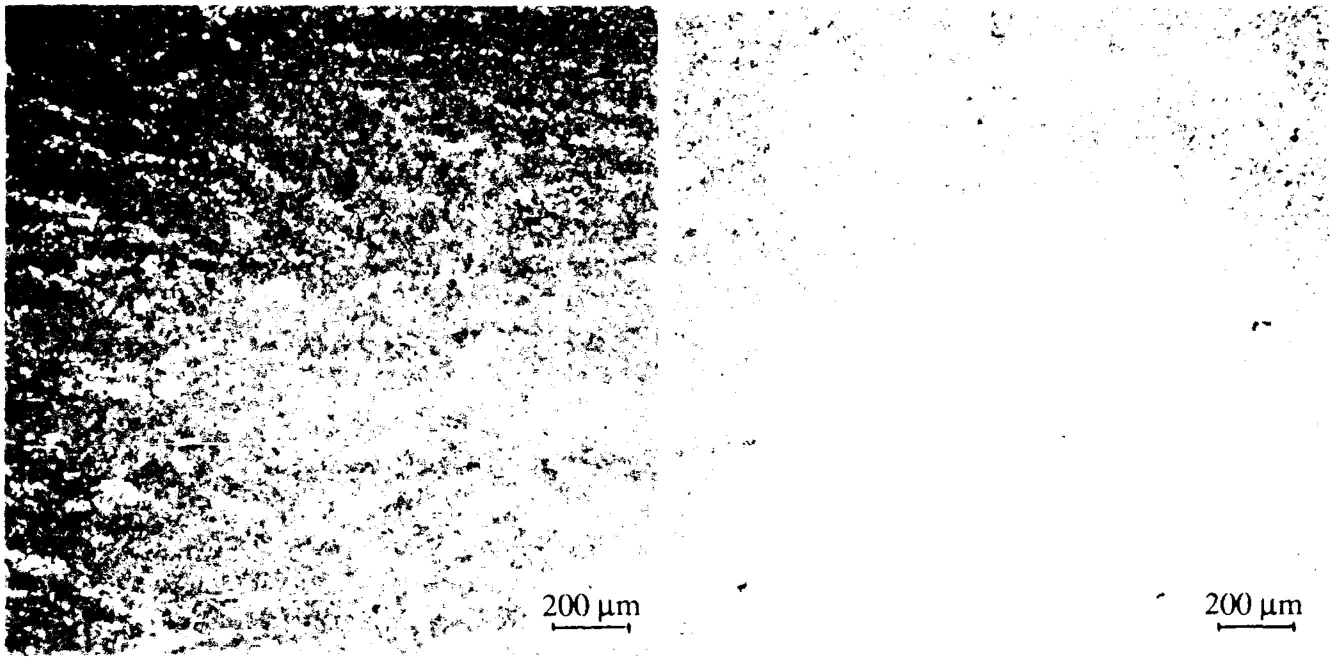
200 μm
200 μm

(a) A2 (b) T2

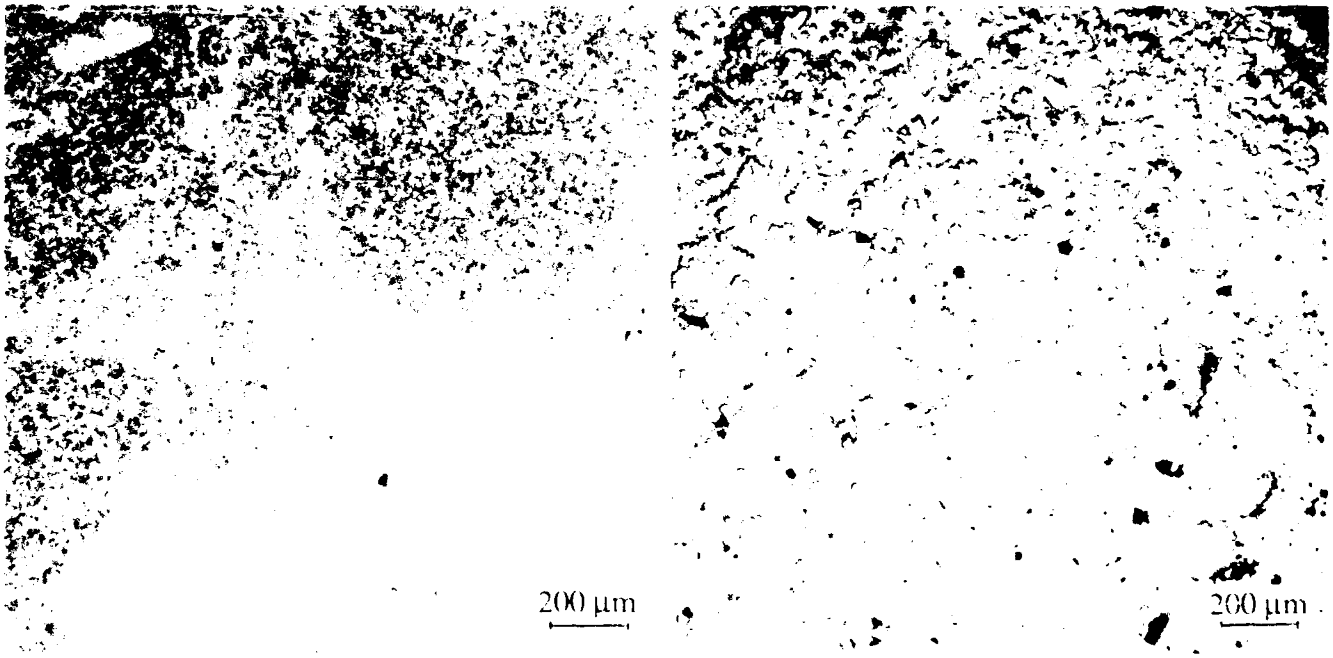
200 μm
200 μm

(c) AMI 2 (d) LANL 2

Figure 1. Macroscopic views of relative composite heterogeneity; compression axis horizontal, lying within hot pressing plane.

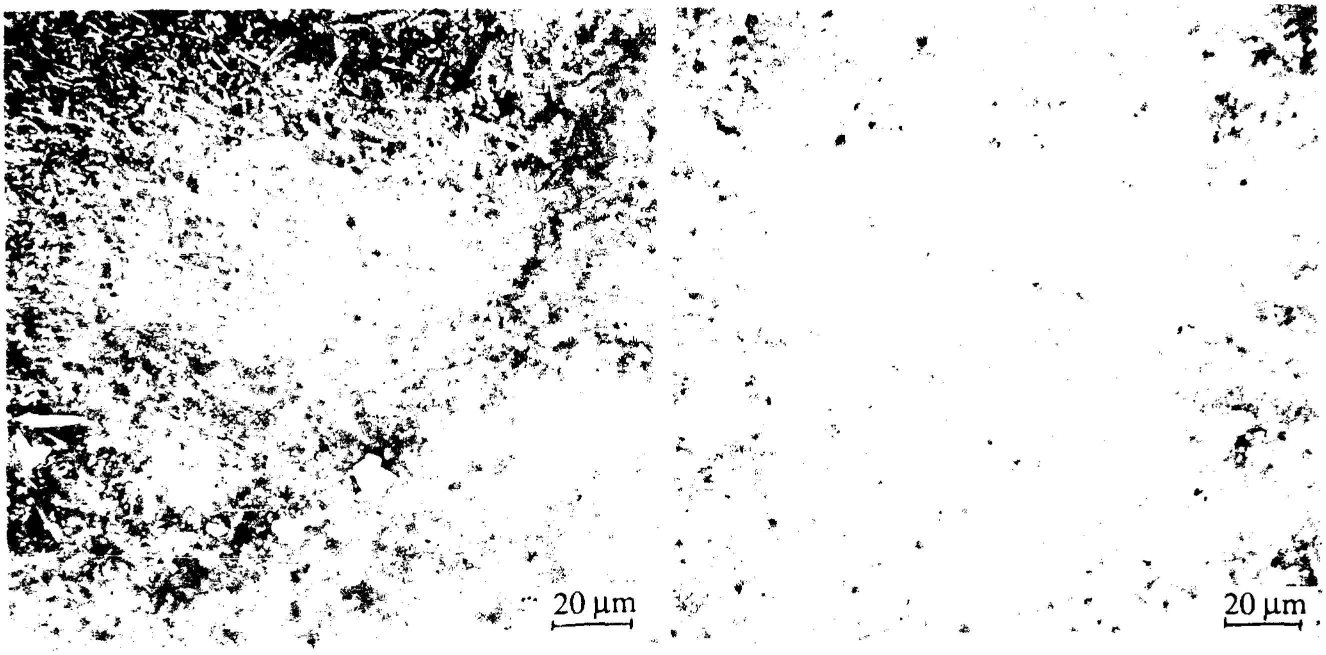

(a) A2 (b) T2

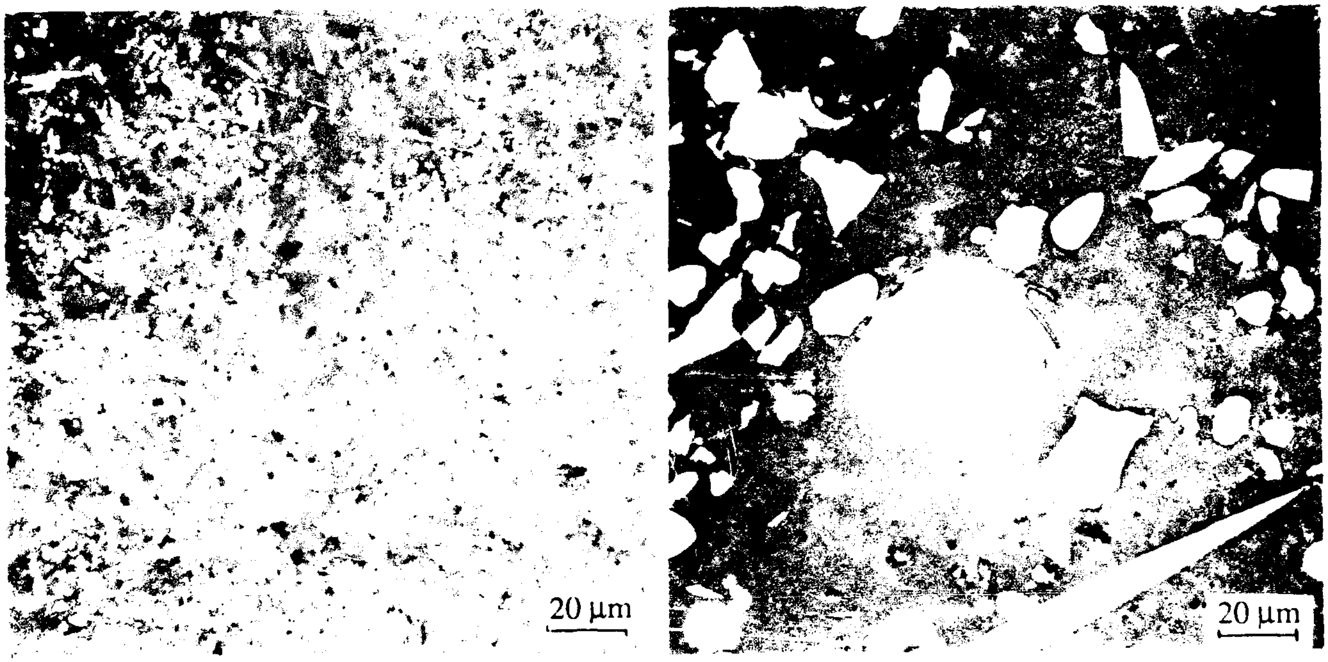

(c) AMI 2 (d) LANL 2

Figure 2. Microscopic views of whisker size, shape, and distribution; compression axis horizontal, lying within hot pressing plane.

III. EXPERIMENTAL PROCEDURES

Cylindrical specimens for compression testing were sectioned from blanks provided by UTRC, with the compression axis lying within the hot-pressing plane (Figures 1 and 2). The samples, as well as high strength alumina* loading platens, were ground and lapped parallel to within 5μm across the 6.5 mm width of the 13 mm long specimens.

Using a standard, but carefully aligned, servo-controlled hydraulic test machine, strain rates ranging from approximately $10^{-4}s^{-1}$ to $2s^{-1}$ were realized. At the lower of these, it was possible to utilize acoustic emission to detect the onset and monitor the development of microcracking. The acoustic emission transducer was resonant at 160 kHz, and its input was filtered to provide a sampling domain of 100 kHz to 1 MHz.

Dynamic compression tests were performed using a split Hopkinson pressure bar (SHPB), which yielded strain rates ($\dot{\varepsilon}$) derived from the stress rate ($\dot{\sigma}$) of the incident stress pulse according to $\dot{\varepsilon} = \dot{\sigma}/E$, where E is the elastic modulus. The rapidity of these tests (<10 μs) precluded the implementation of acoustic emission.

Failed specimens consisted of a multitude of microscopic fragments. Samples of these were mounted and coated with gold for scanning electron microscopy (SEM). In addition, an effort was made to monitor the development of microcracking by studying damaged but unfailed specimens. This was accomplished by loading samples quasi-statically ($\dot{\varepsilon} \cong 10^{-4}s^{-1}$) to stress levels as high as 95% of the compressive strength, σ_c, and then rapidly unloading them to prevent failure. Since observation by SEM failed to reveal microcracking, the specimens were reloaded to a compressive stress of about 0.75 σ_c, held at that level, and replicated to record the presence of previously nucleated microcracks opened up by the moderate applied load.

---

* AD 999, Coors Porcelain Co., Golden, Colorado.

IV. RESULTS

Mechanical Behavior

Stress-strain response was similar for both as-pressed and ceramed composites, examples of which are shown in Figures 3 and 4 for both Arco and LANL whisker-reinforced material. For specimens whose strength exceeded approximately 1200 MPa, a clearly defined yield point was measured (Figure 3); this value varied from 1250 MPa to 1400 MPa for A1, A2, T1, and T2. On the other hand, the deformation of AMI and LANL based composites was linear elastic (Figure 4). In all cases, acoustic emission was not detected until failure was eminent, so that the acoustic emission stress level σ_{AE} was nearly equal to σ_c. The latter behavior was remarkably different from that of pure pyroceram, shown in Figure 5. Here it is evident that although the ceramic yields in a fashion similar to that of the stronger composites, acoustic emission occurs early (relative to σ_c) and abundantly. As for the composites, there is no correlation between σ_{AE} and σ_y.

Strength as a function of strain rate for all the materials is summarized in Figures 6 and 7. Since the matrix material was studied in the ceramed state, it is included with the ceramed composites (Figure 7). The materials clearly are basically strain rate insensitive over the range of the tests, so that it is possible for purposes of comparison to consider each composite as possessing an approximately singular strength.

Thus, for both matrix microstructures, the Tokai and Arco (smaller whisker) variants are significantly stronger than the AMI and LANL whisker-reinforced material. The base pyroceram possesses a strength (Figure 7) intermediate to that of A2/T2 and AMI 2/LANL 2. In all cases, the compressive strength of the as-pressed composites exceeds that of corresponding ceramed variants. Furthermore, this superiority is most marked for the stronger materials, as shown along the left-hand edge of Figure 7. The relative declines in strength effected by the glassy-to-crystalline transformation are indicated for $\dot{\varepsilon} \cong 10^{-5}s^{-1}$. While the strength of Tokai and Arco reinforced material drops precipitously, that of the LANL reinforced material is virtually unaffected.

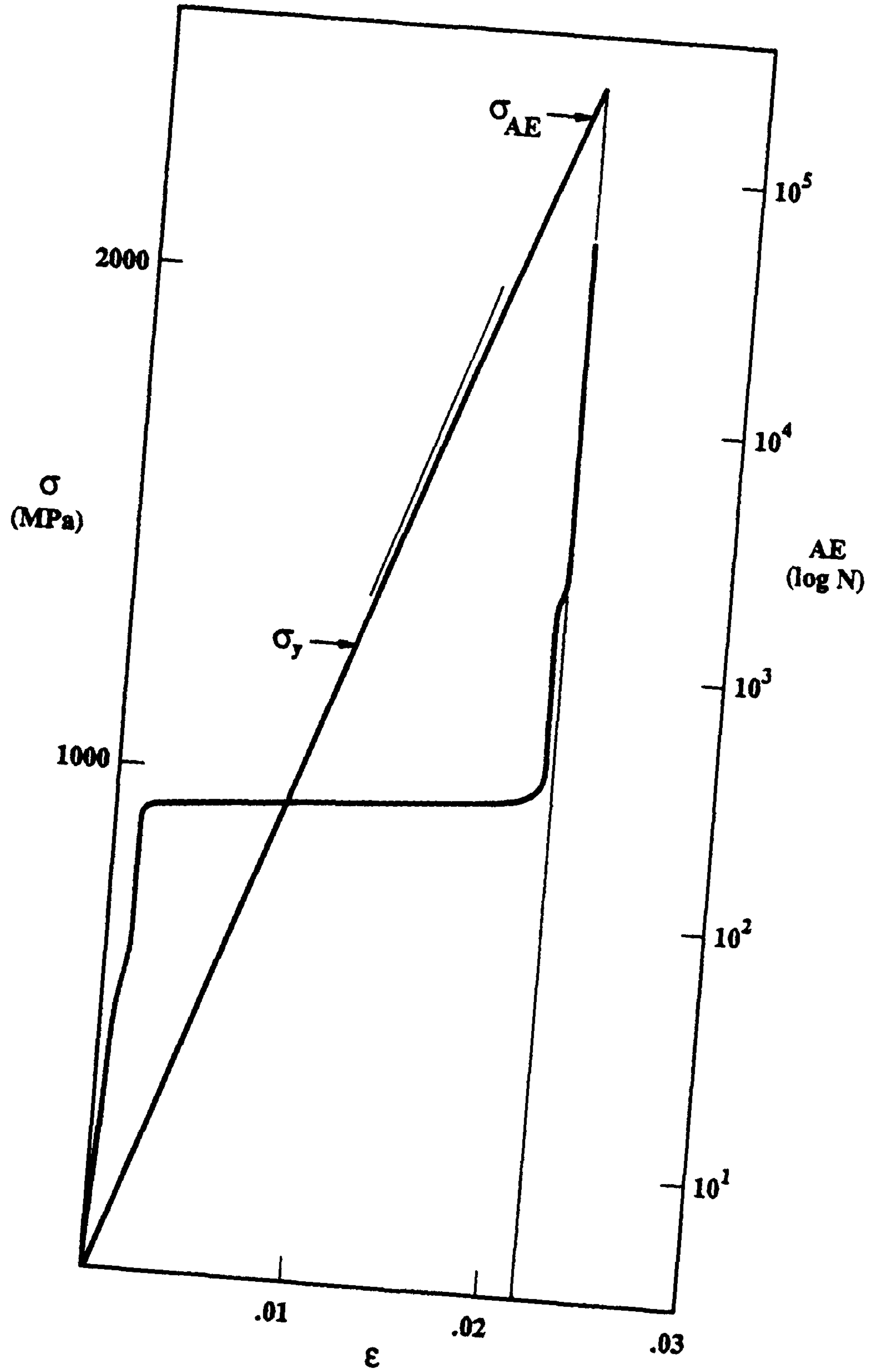

Figure 3. Stress and Acoustic Emission Versus Strain for A2 at $\dot{\varepsilon} = 3.2 \times 10^{-4} s^{-1}$.

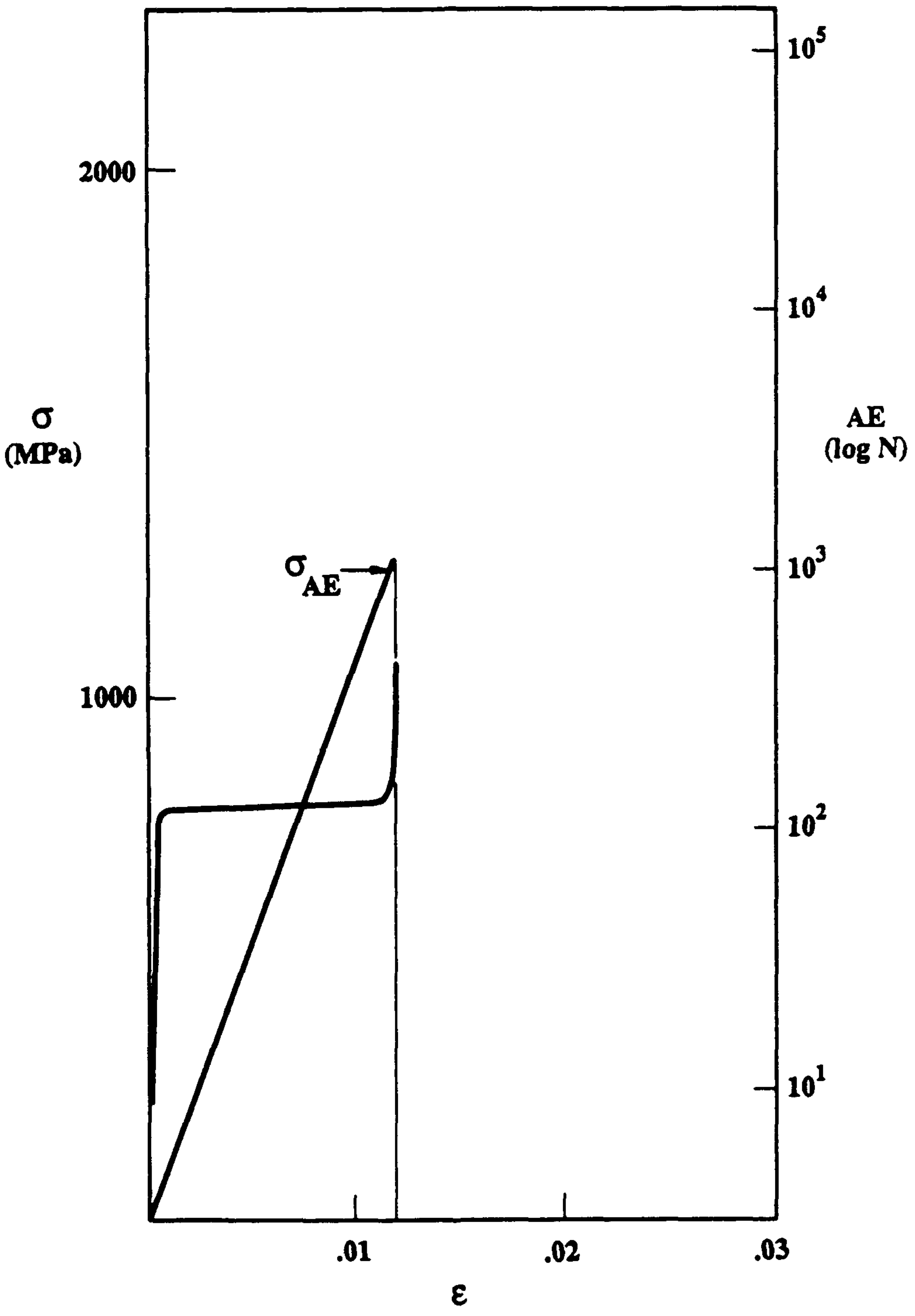

Figure 4. Stress and Acoustic Emission Versus Strain for LANL 2 at $\dot{\varepsilon} = 2.8x\,10^{-4}s^{-1}$.

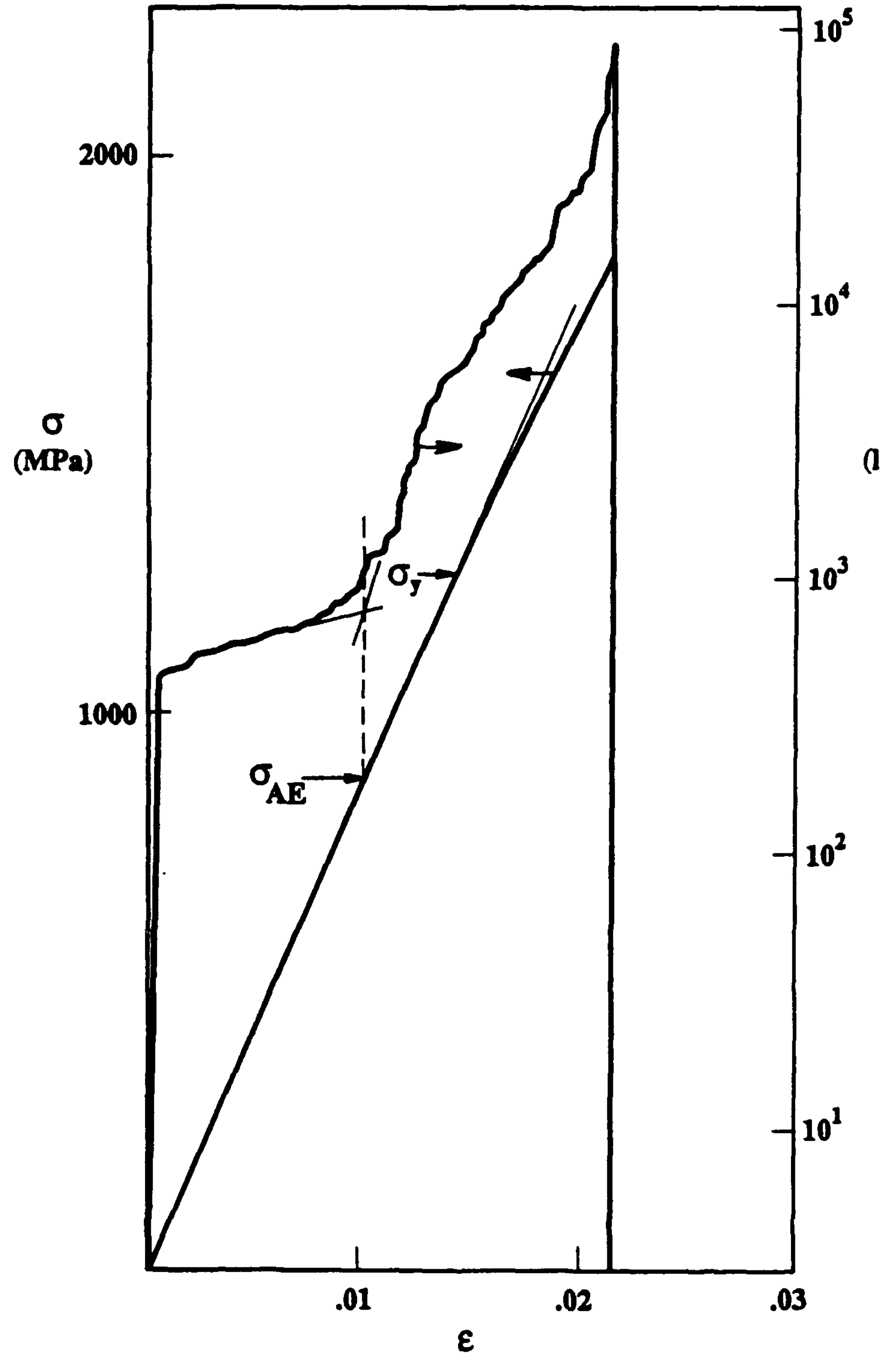

Figure 5. Stress and Acoustic Emission Versus Strain for Pyroceram at $\dot{\varepsilon} = 1 \times 10^{-4} s^{-1}$.

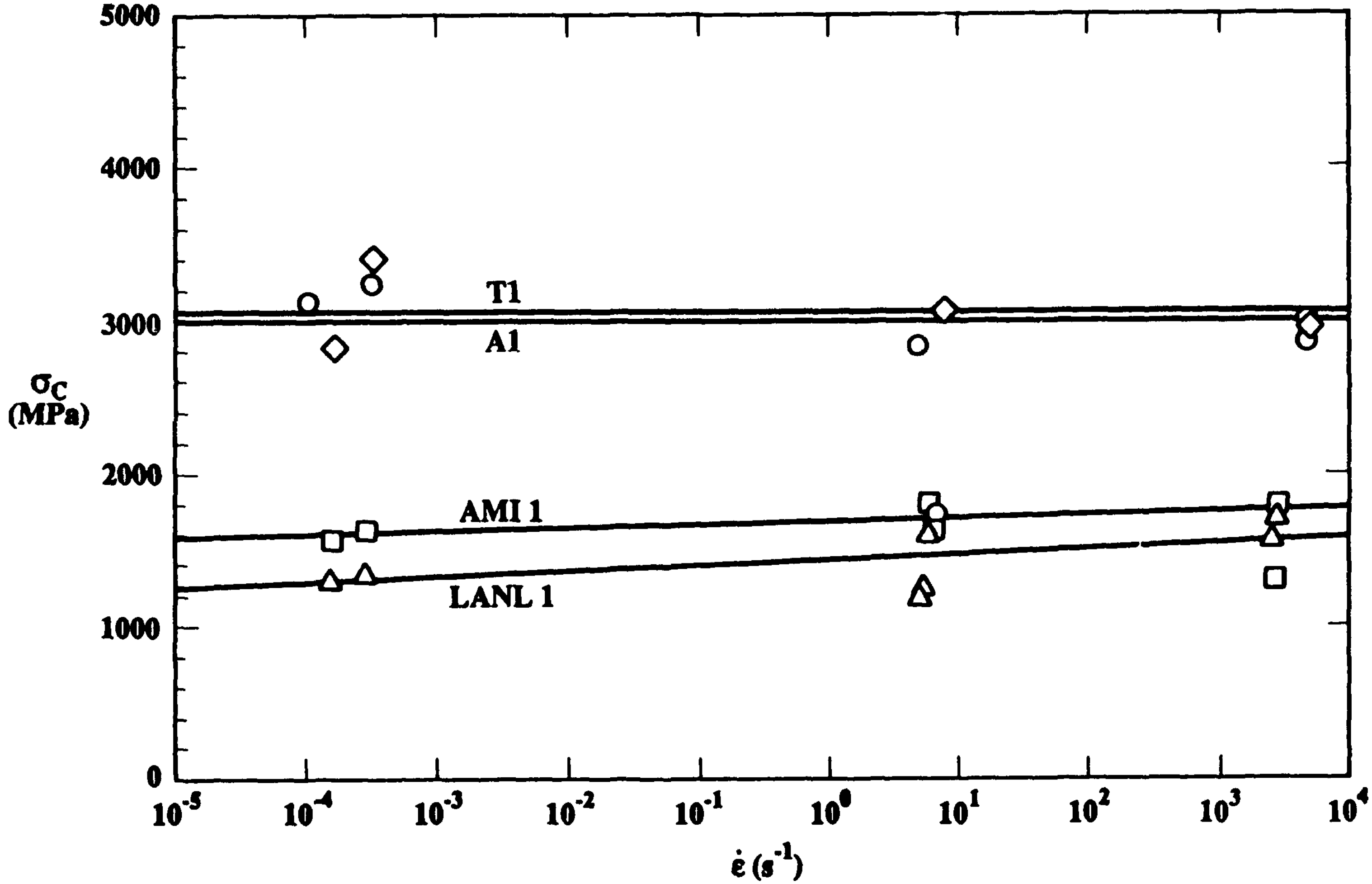

Figure 6. Compressive Strength Versus Strain Rate for As-Pressed Composites.

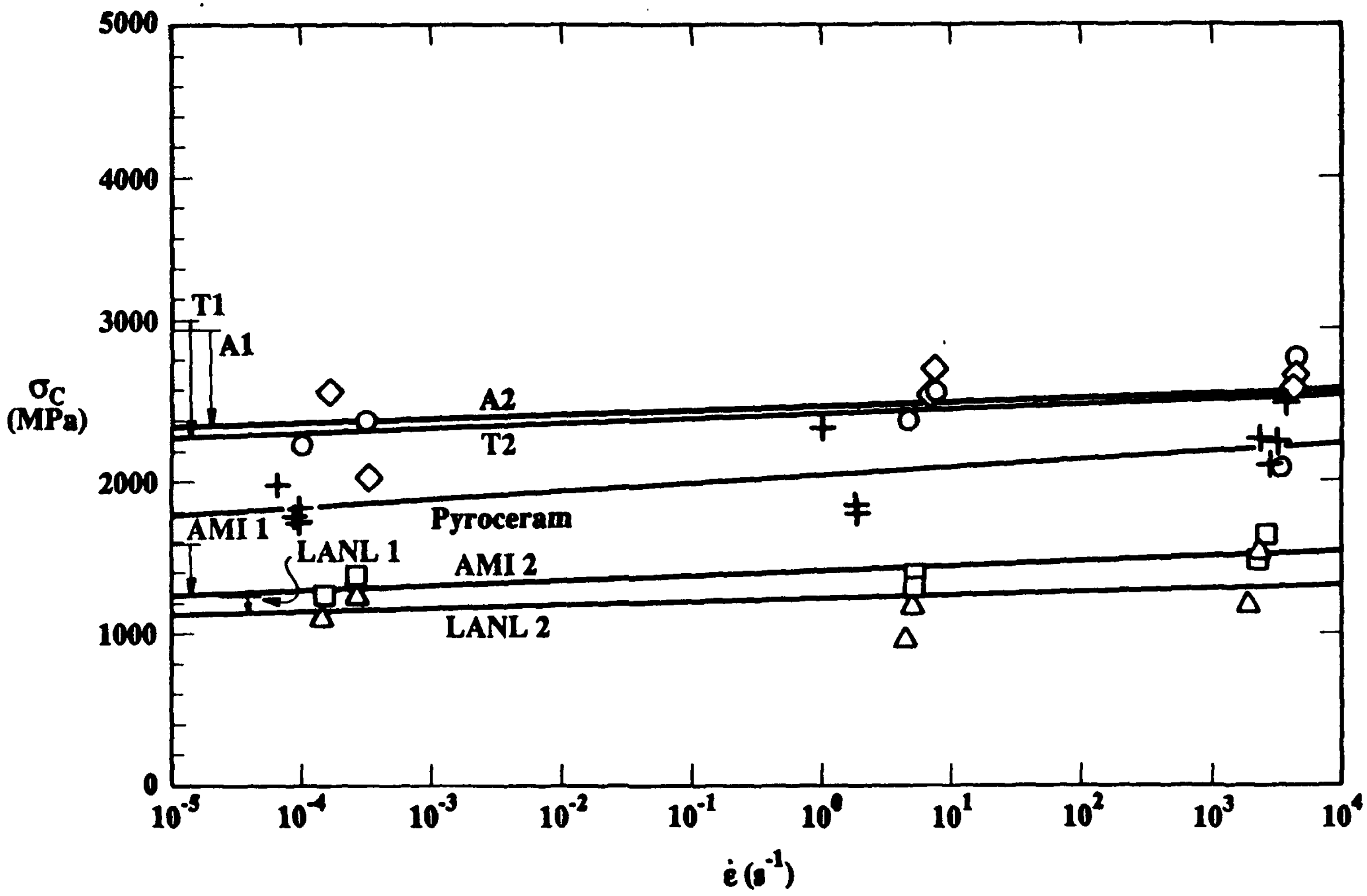

Figure 7. Compressive Strength Versus Strain Rate for Ceramed Composites and Pyroceram.

Fracture Characteristics

Characterization of the damage state in specimens loaded nearly to failure proved difficult. Only for LANL 2 material was it possible to detect microcracks, some of which are shown in Figure 8, representing a specimen loaded to 95% of its nominal compressive strength at a strain rate of approximately $10^{-4}s^{-1}$. Based on Figure 8(a), it appears that the axial microcrack has nucleated at the surface of a large whisker, as indicated by the arrow. On the other hand, once a crack in this system has nucleated, it seemingly does not subsequently experience significant interaction with those whiskers which it may encounter [Figure 8(b)].

The preceding inferences are strongly supported by SEM study of the fracture surfaces of specimen fragments, and a number of other factors are revealed. Figure 9, for example, shows the fracture modes characteristic of quasi-static loading rates for two extremes in (strength) behavior, i.e., Arco and LANL reinforced material, with the matrix in both the as-pressed and ceramed conditions. For both whisker variants, fracture of the as-pressed material was surprisingly ductile, almost "viscous" [Figure 9(a and c)], while in the ceramed state, failure occurred in an obviously brittle fashion [Figure 9(b and d)]. Fracture of the Arco composite evidences both fiber pullout, in the form of fiber-shaped (rounded triangular) holes, and crack deflection around fibers [Figure 9(a and b)]; similar features were observed for T1 and T2 material. No such pullout occurred for either the LANL [Figure 9(c and d)] or the AMI composite.

At high strain rates, the fracture appearances were similar, except that the "viscous" nature of as-pressed material became much more "brittle" (Figure 10), resembling that of the ceramed variants [Figure 9(b)]. Whisker pullout was still observed for the Arco and Tokai reinforced LAS, and crack deflection by whiskers lying in the crack plane (Figure 10) was quite pronounced.

A few specific details seem worthy of mention. The "viscous" fracture mode characteristic of as-pressed material at lower rates of loading is clearly evident in Figure 11. The appearance is

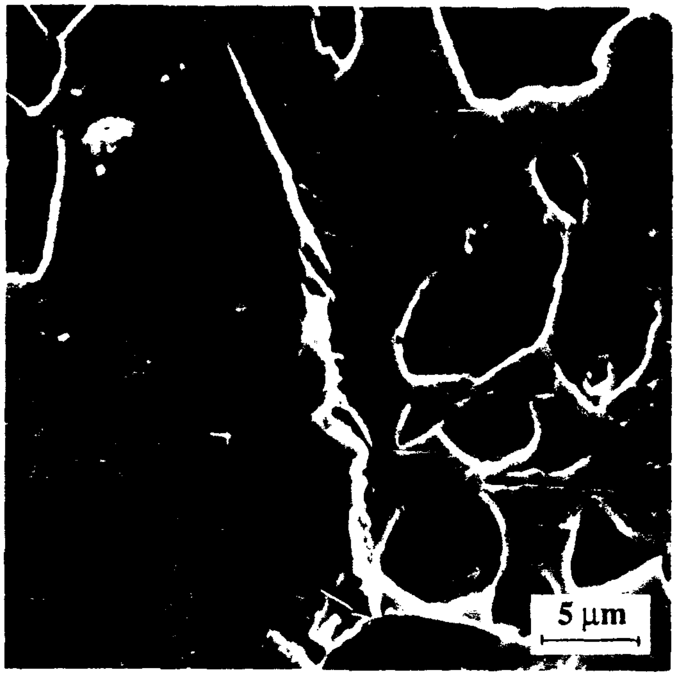

(a) Cracked nucleated at large whisker (arrow).

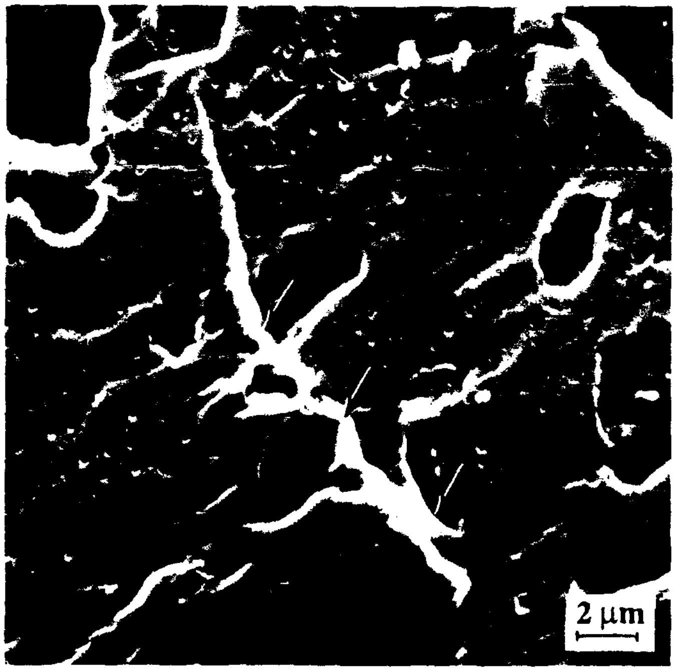

(b) Crack non-interaction with adjacent whiskers (arrow).

Figure 8. Early stages of compressive microfracture in LANL 2, $\dot{\varepsilon} \cong 10^{-4}s^{-1}$, $\sigma = 0.95\ \sigma_C$; compression axis vertical.

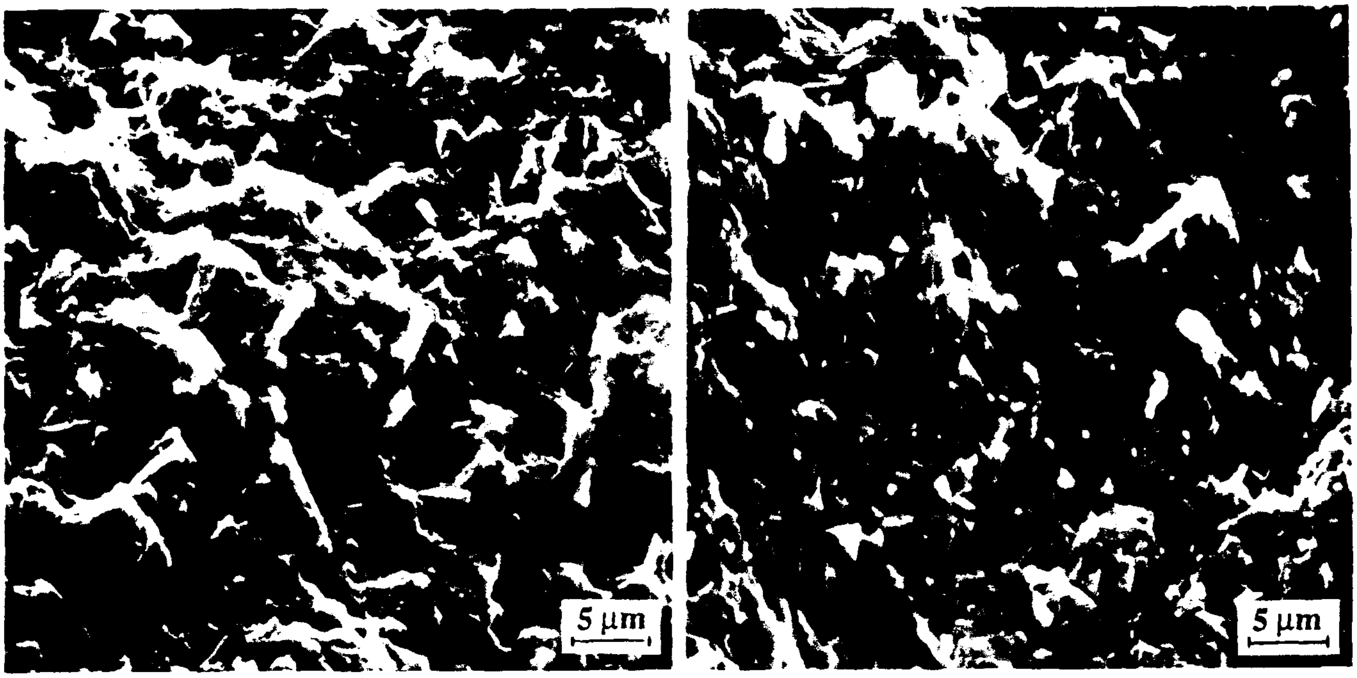

(a) A1 (b) A2

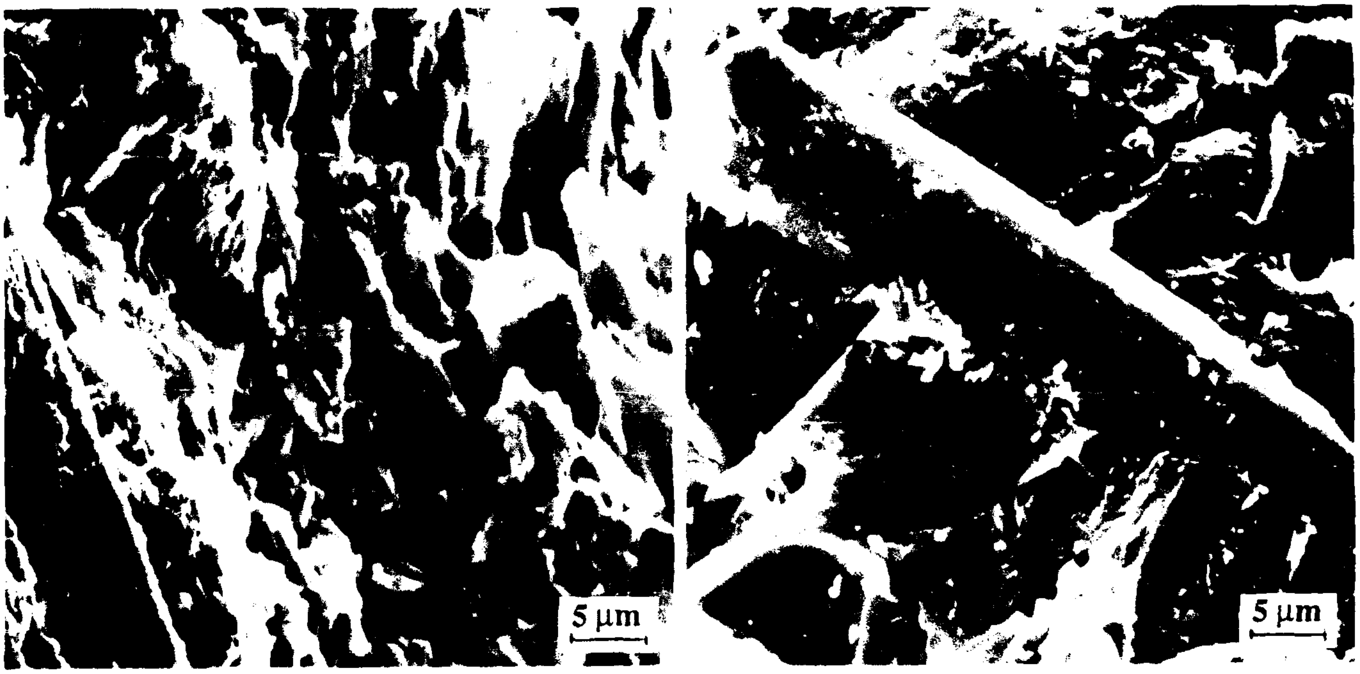

(c) LANL 1 (d) LANL 2

Figure 9. **Fracture surfaces, Arco versus LANL whiskers, as-pressed and ceramed, $\dot{\varepsilon} \cong 10^{-4}s^{-1}$.**

that of ductile hole growth by the formation of local tensile ligaments which fail by necking. It is hardly necessary to observe that this is an uncommon failure mechanism for any ceramic (albeit a "glassy" one) under quasi-static, ambient conditions.

Finally, a frequently observed fractographic feature in the LANL and AMI composites was the presence of matrix microcracks associated with whiskers, with the crack plane oriented parallel to the whisker axis. Figure 12 shows such a microcrack nucleated at the whisker-matrix interface, the conformation of the crack being that of a classic half-penny.

V. DISCUSSION

Probably the most striking aspect of the present results is the range of strength values obtained, and the fact that they tend to lie above and below the strength of pyroceram material, which is extremely similar in chemistry and microstructure to the matrix material. It is possible to rationalize this behavior in terms of the specific influence of the reinforcing whiskers, which can manifest themselves in several ways, depending on their relative size, spacing, and ability to interact with the matrix.

For example, it is clear from the acoustic emission results that the presence of the Arco and Tokai whiskers serves to suppress the strong tendency of the matrix to damage itself by prolonged pre-failure (recall Figures 3 and 5) microfracture. Although some evidence of whisker pullout was seen, this cannot be the origin of the suppression of microcrack initiation, since the frictional pullout mechanism presupposes the existence of a whisker-bridged matrix crack. Thus, it seems much more likely that the whiskers retard the onset of crack nucleation through a network of residual stresses generated by whisker-matrix thermal expansion mismatch. The concept of a network is based on the fact that for the same whisker volume fraction, the whisker/matrix "unit cell" will be much smaller than that of composites reinforced with the larger AMI and LANL whiskers. In the latter case, the whiskers are sufficiently far apart [Figure 9(d)] that large volumes of matrix are basically unreinforced.

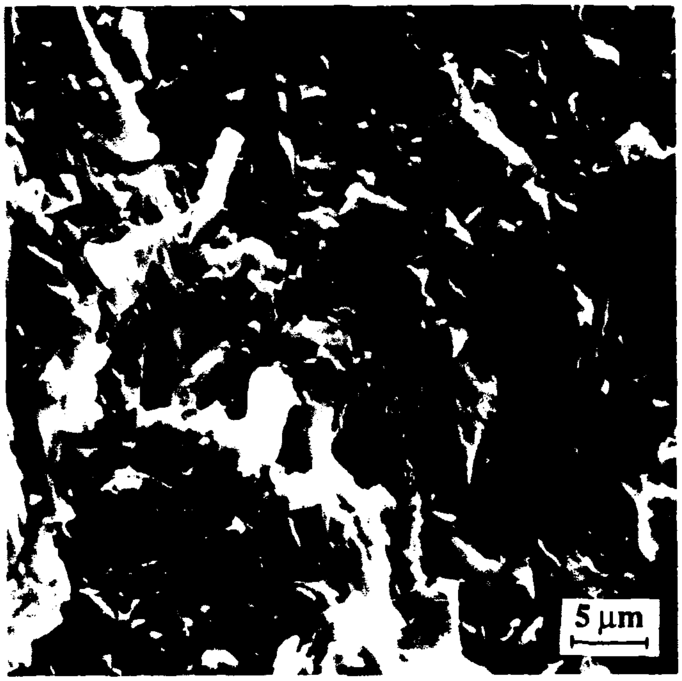

Figure 10. Fracture surface of A1 at $\dot{\varepsilon} \cong 2000s^{-1}$. Note evidence of crack deflection, in the whisker-shaped crevices left by whiskers attached to the mating surface.

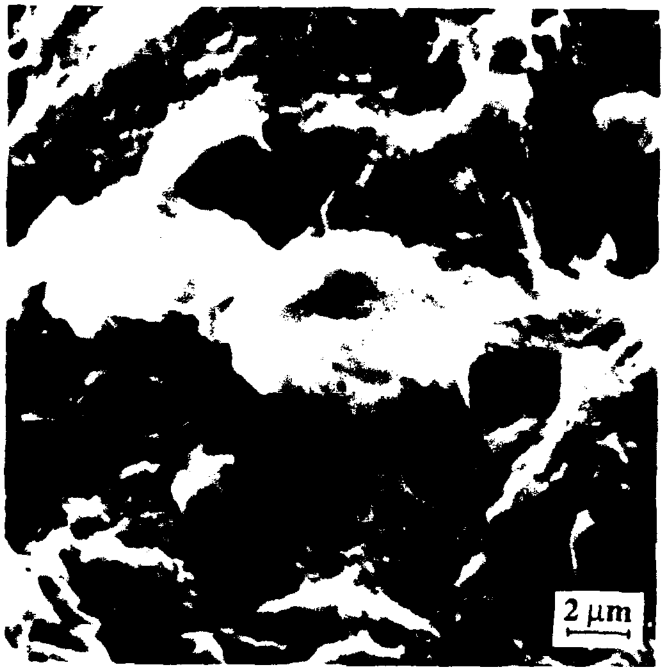

Figure 11. Viscous fracture mode in A1 tested at $\dot{\varepsilon} \cong 10^{-4}s^{-1}$.

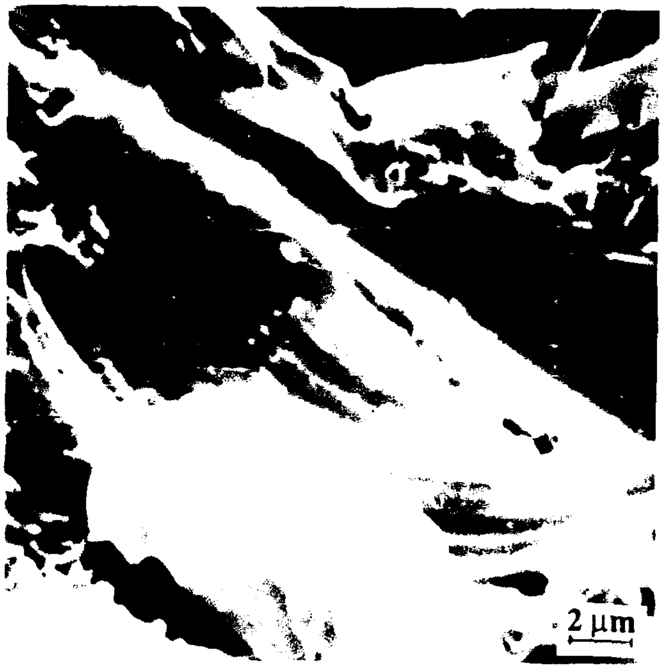

Figure 12. Whisker-initiated microcracking in LANL 1 at $\dot{\varepsilon} \cong 10^{-4}s^{-1}$.

Moreover, it was shown (Figure 12) that the large whiskers actually are detrimental, in that they are potent crack nuclei. Under compressive loading, being much harder than the matrix, they act as micro-indenters, producing axially oriented, (locally) tensile microcracks. This would also be the case for the smaller Arco and Tokai whiskers as well, but the microcracks would be smaller, since the size of the local tensile field would scale with whisker diameter.

The hypothesis that residual stresses are responsible for the good (relative to pyroceram) performance of the Arco and Tokai whisker reinforced material is supported by the fact that it is for these systems that the greatest strength differential is observed upon heat treating the as-pressed material to the ceramed state. This process would in no way change whiskers, but it would tend to alter, evidently in the compressive direction, the global residual stress field. Similarly, the minimal strength differential for as-pressed and ceramed AMI and LANL whisker composites suggests that the dominant role is played by the crack nucleating "inclusion" nature of the large whiskers.

Although the apparent "viscous" fracture capability of the as-pressed material is surprising and interesting, it does not seem very important, compared to residual stresses and whisker crack nucleating capabilities. If it were significant, it would be expected that as the strain rate increased, the strength of the as-pressed material would rise or fall versus that of the ceramed material. Clearly (Figures 3 and 4), that is not the case.

The ceramed-state fracture features observed in these experiments are qualitatively similar to those characterized by Brennan[5] for identical material failed in flexure. His conclusions regarding the relative roles of whisker pullout and crack path tortuosity are borne out, reinforcing the fact that the compressive failure mode is in reality a series of more-or-less simultaneous local tensile microcrack nucleation events, producing an ensemble of axial cracks which coalesce to produce failure.

The absence of a dynamic strain rate strengthening effect in the present experiments stands in stark contrast to the intense rate sensitivity obtained[4] in SHPB tests of SiC whisker reinforced, as well as unreinforced, hot pressed Si_3N_4. Considering these two extreme cases, it is evident that the presence of reinforcing whiskers does not significantly affect dynamic response; rather, it must be understood as a function of the matrix phase alone. This is not true for fiber reinforced ceramics (such as SiC fiber reinforced LAS[6]), in which case the micromechanics of dynamic failure are remarkably different for the composite versus the matrix.

VI. ACKNOWLEDGEMENTS

The author is grateful for the support of the Office of Naval Research under Contract No. N00014-84-C-0213. The kink provision of the whisker-reinforced blanks by J. J. Brennan of UTRC is gratefully appreciated as is the careful experimental work by A. Nicholls.

VII. REFERENCES

1. S-T. Buljan, A. E. Pasto, H. J. Kim, *Am. Ceram. Soc. Bull.*, **68** (1989) 387.

2. G. C. Wei and P. F. Becher, *Am. Ceram. Soc. Bull.*, **64** (1985) 298.

3. P. F. Becher, *Acta Metall.*, **34** (1986) 1885.

4. J. Lankford and C. R. Blanchard, *Mat. Sci. Eng.*, (in press).

5. J. Brennan, "Interfacial Studies of Whisker Reinforced Ceramic Matrix Composites," Annual Report R89-917894-1, AFOSR Contract. No. F49620-88-C-0062, May 31, 1989.

6. J. Lankford, *Ceram. Eng. Sci. Proc.*, **9** (1988) 843.

Submitted to Journal of the American Ceramic Society

III.

EFFECT OF DYNAMIC LOADING ON TENSILE STRENGTH AND FAILURE MECHANISMS IN A SIC FIBER-REINFORCED CERAMIC MATRIX COMPOSITE

J. Lankford, H. Couque, and A. Nicholls
Department of Materials Sciences
Southwest Research Institute
6220 Culebra Road
San Antonio, Texas 78228-0510

ABSTRACT

The tensile strength and associated failure micromechanisms have been characterized for a SiC fiber-reinforced ceramic matrix composite subject to strain rates approaching $1000 s^{-1}$. It is found that behavior under such conditions is not described by the current matrix fracture/fiber pullout models. This is a consequence of the rapid and extreme frictional heating produced at the fiber-matrix interface by sliding velocities on the order of 100 m/s. At sufficiently rapid loading rates, the near-interface matrix appears to virtually melt, and the frictional interface shear resistance is reduced to the point that the fibers debond throughout the specimen, and pull out without failing. This suggests that for sufficiently rapid loading, the stress to fail the composite will approach that merely to create the initial matrix crack, i.e., a stress level well below the ultimate strength normally attainable under quasi-static conditions. [Key words: dynamic fracture, tensile fracture, composites, glass ceramics, fibers, interfacial friction.]

I. INTRODUCTION

Ceramic matrix composites reinforced with silicon carbide fibers currently are candidates for a variety of applications in which their nominal material and mechanical properties appear to be extremely desirable. However, an important performance consideration, i.e., their response to dynamic, or impulsive, tensile loading has not yet been explored, either theoretically or experimentally. This factor surely will be highly relevant to a number of potential applications, and deserves careful study.

This is not to say that the effect of loading rate, per se, on fiber-matrix interaction has not received study; in fact, it has. Goettler and Faber[1], for example, have shown that the interfacial shear strength within the SiC fiber-borosilicate glass system increases with stress rate. On the other hand, Philips[2] has observed that both the work of fracture and fiber pullout length are constant with increasing rate of loading for carbon fiber-reinforced LAS pyroceram. However, it should be noted that the fiber sliding rates in these experiments were low, on the order of 10^{-7} - 10^{-4} m/s. Under the rapid loading conditions envisioned here, fiber sliding rates may attain velocities as high as 100 m/s. In this regime, factors other than those which control slow crack growth (such as moisture-assisted stress corrosion) are expected to dominate.

The mechanisms responsible for the excellent and unusual (for a ceramic) quasi-static strength, deformation, and toughness of fiber-reinforced ceramics have been thoroughly reviewed recently by Evans and Marshall[3]. Basically, "good" fiber-reinforced ceramics exhibit tensile stress-strain behavior as shown schematically in Figure 1. The initial deviation from linearity (σ_O) corresponds to the formation of the first crack in the matrix, which extends entirely across the specimens, breaking very few fibers en route. With increased loading, other matrix cracks are initiated, separated by a spacing characteristic of the frictional stress transfer afforded by the fiber-matrix interface. Further non-linear deformation is produced by unbroken fibers sliding within these crack-created "blocks" of matrix material. Once the specimen gage section is full of cross-sectional matrix cracks, the surviving fiber bundles begin to fail, i.e., the ultimate strength (σ_U) has been attained. Any further tail in the stress-strain curve is caused by broken fiber pullout. This mechanism has been validated,[3-6] but only for what amounts to quasi-static rates of loading.

The specific parameter that determines the rate of load transfer from the fibers to the matrix, and thus the ultimate strength of the composite, is simply the frictional resistance to fiber "pullout."

For micromechanics purposes, it is convenient to treat the latter as an effective shear stress, τ, characteristic of a debonded interface. However, from a materials response viewpoint, it is more relevant[3] to view τ (to a first order) as μq_N, where μ is a classic friction coefficient, and q_N is the residual stress normal to the interface. Thus, the question at issue reduces to the effect of dynamic loading upon μ and q_N.

Study of sliding friction between ceramic couples indicates that μ generally increases with sliding velocity; such behavior is primarily a consequence of the interfacial temperature rise associated with rapid sliding. Under steady state sliding conditions, the local temperature may rise hundreds of degrees,[7] promoting local plasticity and thermal expansion. For the case of fibers sliding within a confined space, thermally-induced dimensional changes would tend to alter q_N, while the softening of interface constituents, permitting frictional energy-absorbing plasticity, would be reflected in μ. In this regard, it is relevant to note that for LAS pyroceram couples sliding under ambient conditions, an increase in the sliding velocity from 0.5 m/s to 1.8 m/s doubled the friction coefficient.[7] After 500s of sliding at each velocity, corresponding near-interfacial temperatures were 110° and 450°C, respectively. Moreover, measurements of fiber displacement caused by quasi-static microhardness indentation indicate[8] that for strong, tough SiC fiber-reinforced pyroceram, the fiber/matrix friction coefficient may be as low as 0.01; under these circumstances, i.e., low sliding velocity, frictional temperature increases are negligible. However, in light of the apparent small amplitude of μ, combined with its major role in the composite failure process, it is clear that changes induced in it by dynamic loading could have a profound effect on both strength and (effective) ductility.

The objective of the present work is to explore the effect of high strain rates upon the tensile failure process in a representative fiber-reinforced ceramic matrix composite. It will be seen that the results indeed must be interpreted in terms of thermal effects at the fiber/matrix interface.

II. MATERIAL

The composite chosen for study was fabricated* by United Technologies (UTRC), and has been characterized microstructurally by Brennan.[10] Briefly, the panel from which the specimens were extracted was laid up unidirectionally using 46 v/o Nicalon silicon carbide fibers; the latter are approximately 16 μm in diameter. The matrix was the UTRC lithium-aluminosilicate glass ceramic designated as LAS-II, which is essentially Corning 9608 pyroceram modified by replacing 3 w/o TiO_2 with 3 w/o ZrO_2, and adding 5 w/o Nb_2O_5. After fabrication, the composite is "ceramed," or crystallized, by heat treatment at 1,050°C for two hours. The resulting matrix consists of grains ranging in size from ~ 0.5-2.0, crystallized in the β-quartz-silica solid solution LAS phase. However, the microstructure is different near the fiber-matrix interface: next to the fiber is an extremely thin layer of eta aluminum, contained within an adjacent matrix ring of very fine NbC precipitates. In addition, the fibers themselves are altered by the processing, their outer layer consisting of a 200-400Å thick ring of almost pure carbon. This carbon-rich zone is weakly bonded to both the matrix and the fiber, and is thought[8] to be responsible for the low value of the quasi-static fiber-matrix sliding friction coefficient.

III. EXPERIMENTAL PROCEDURES

Mechanical Testing

Test coupons with fibers parallel to the tensile axis were sectioned from plate material; in this form, the coupons consisted of simple cylinders 35 mm long and 3 mm in diameter. (Because of limitations on material availability, it was possible to fabricate a total of only four such cylinders. However, it will be shown that the experimental results obtained are sufficiently distinct in their phenomenology to be considered representative of the particular test conditions imposed.) The coupons were modified by using a shaped grinding wheel to generate a reduced midsection characterized by an 8.9 mm gage length and a 2.05 mm diameter. These specimens were then bonded into internally threaded steel sections, using high strength epoxy.

---

* Panel 2391, Ref. 9.

The quasi-static experiment was performed using a standard servo-hydraulic test machine under displacement control at a constant strain rate of $10^{-5}s^{-1}$. However, to promote pure axial loading, load transfer was accomplished by means of thin, flexible, steel cables (Figure 2) threaded into the specimen grips. Strain was measured over the entire specimen using an extensometer.

Dynamic tensile tests utilized a split Hopkinson pressure bar (SHPB) modified for tensile testing.[11] The test set-up consists of a split collar placed about a button head tensile specimen as shown in Figure 3. An incident compressive stress wave, generated from the impact of a projectile striker bar at one end of two long bars in series, is transmitted through the insert from one bar to the other, leaving the specimen intact. A tensile wave is then reflected from the free end of the SHPB, causing the specimen to be loaded in tension. Axially-symmetric play of each thread of the tensile specimen is ensured by means of a teflon guide. From the strain record of the transmitted and reflected pulses in the pressure bars, the stress and the strain rate, respectively, are deduced,[1] and by integrating the strain rate with respect to time, strain versus time is generated. The stress-strain curve is finally obtained by eliminating time. The strain record includes the deformation of both the specimen gage section and the bonding film between the specimen and the steel insert. An estimate of the strain within the bonding film was obtained based on photographs of the specimen/insert junction before and after testing. The value found (< 0.002) indicates that the elastic strain (about 0.02) in the specimen was measured with an error of less than 10 percent.

Since it will be seen that the present composites are "ductile" under certain conditions, it should be noted that when this happens, the dynamic strain rate is not constant. Initially, a constant stress rate ($\dot{\sigma}$) ramp is imposed, lasting for approximately 10-20 μs; during this regime, the strain rate $\dot{\varepsilon}$ is equal to $\dot{\sigma}/E$, where E is the elastic modulus of the composite. However, should the specimen yield, the strain rate will instantaneously increase due to the lower (effective) modulus, and will be reflected in the stress-time history recorded by the SHPB strain gages. It should be noted that the elastic strain rate can be varied somewhat by controlling the velocity of the striker bar; in particular, the stress rate increases with velocity.

Damage Characterization

Failed specimens were examined by optical microscopy, specifically to provide a measure of the spacing of any matrix microcracks. In addition, fracture surfaces were coated with gold, and subjected to scanning electron microscopy (SEM).

IV. RESULTS

Deformation behavior is summarized in Figure 4. Almost hidden in the initial rise of the high strain rate curves lies the complete quasi-static stress-strain response; in all the SHPB experiments, the ultimate strength is significantly higher than the quasi-static value. At the two highest strain rates, however, the strain at failure is drastically reduced versus that which obtains at $\dot{\varepsilon} = 346\text{s}^{-1}$, and there is no obvious yield point. *Failure at the latter rate is followed by an extensive regime of* continuously declining strength, while in the higher rate dynamic experiments, the post-failure region consists of a series of minor stress-strain peaks of declining amplitude.

Considering the stress-strain curves of the two specimens which were characterized by a "yield" point (Figure 5), it is evident that σ_O for both $\dot{\varepsilon} = 1.15 \times 10^{-5}\text{s}^{-1}$ and 346s^{-1} is roughly the same, although it is not as accurately defined for the higher rate test (a best fit curve has been drawn through the oscillations, which are typical of the early portions of SHPB flow stress curves). On the other hand, while it is possible to achieve a permanent strain of approximately 0.001 at a strain rate of $1.15 \times 10^{-5}\text{s}^{-1}$, a plastic strain of nearly 0.03 is attained when $\dot{\varepsilon} = 346\text{s}^{-1}$.

Optical examination revealed within the latter failed specimens periodic matrix microcrack ensembles previously identified as characteristic of, if not required for, non-catastrophic composite failure. Crack spacing data is summarized in Table I, where D is the saturation crack spacing. It should be noted that similar multiple microcracks could not be discerned for the specimens tested at the two highest dynamic strain rates, for which D must be equal to or greater than the specimen gage length.

Table I. Crack Spacing Measurements

$\dot{\varepsilon}$ (s^{-1})	D (μm)
1.15×10^{-5}	310 ± 32
346	515 ± 43
947	≥ 4445
1100	≥ 4445

Fiber pullout was strikingly strain rate dependent, as shown in Figure 6. Under quasi-static conditions (A), the pullout length varied a great deal. As the loading transits to the dynamic regime (B), this variation is reduced, and so is the average pullout length; further reduction in pullout is observed at a still higher strain rate (C). Finally, at the highest strain rate (D), a major change in behavior occurs, i.e., a large number of fibers are pulled out intact, as evidenced by the horizontal coincidence of their originally ground (parallel) ends. It should be noted that this last observation is the physical basis for computing the strain rate attributed to this experiment. Initially, it appeared that the specimen, which on the basis of striker velocity should have endured the highest rate of strain, had not. That is, it did not, when the strain rate was computed in terms of $\dot{\sigma}/E$, which yielded $\dot{\varepsilon} = 897s^{-1}$, versus a rate of 947^{-1} obtained at the next lowest striker velocity. However, since failure of this anomalous specimen was accompanied by extensive unbroken fiber pullout, the fibers clearly did not experience the strain, hence did not contribute the stiffness factor, which they otherwise would have. Thus, the effective modulus (E) of the composite must have been lower than E. Assuming a modulus decrease of 15-20%, the actual strain rate, in this case, would be on the order of $1100s^{-1}$. The latter estimate will be used subsequently in correlating results.

In addition to these macroscopic features, the effect of strain rate on fracture mode is manifest at the microscopic level as well. This is demonstrated in dramatic fashion in Figure 7, where (B) and (D) are typical of the appearance of all the SHPB specimens. At slow rates (A), fibers pull out cleanly, and at high magnification, the fracture surface has a simple cleavage appearance. On the other hand, under dynamic loading (B), fibers are pulled out attended by globular debris; close inspection (D) shows that the latter appears to have solidified from a liquid state. The uppermost particle, in fact, is barely attached by a neck apparently solidified just prior to droplet separation.

V. DISCUSSION

It is apparent that under quasi-static conditions, the composite behaves in the standard way. The observed stress-strain curve (Figure 5(A)) is similar to that reported[9] for identical material tested in a different tensile configuration, and the matrix microcrack spacings (310 μm) are in excellent agreement with those (290 μm) reported[5] for a similar, but not identical Nicalon-LAS system. Based on the wide distribution in fiber pullout length (Figure 6(A)), it is reasonable to assume that the equilibrium nature of the test provided ample opportunity for the stress distribution within the microcracked matrix to sample the statistical flaw distribution within the fiber bundle.

However, the crack spacing is significantly greater (515 μm) at the lowest dynamic loading rate, and apparently is equal to the specimen gage length (at least) for still higher rates. The significance of an increasing crack spacing can be explored as follows. First, it has been shown[5] that the sliding shear stress τ and D are related by

$$\tau = \lambda\,[(1-f)^2\Gamma_m E_f E_m R^2/fED^3]^{1/2} \tag{1}$$

where λ is a quantity equal to 1.34, f is the fiber volume fraction, Γ_m is the matrix fracture energy, R is the fiber radius, and E_f, E_m, and E are the elastic moduli of the fiber, the matrix, and the composite, respectively. Similarly, the threshold stress for matrix cracking can be expressed in terms of a lower bound, steady-state value as

$$\sigma_O = \left[\frac{6\tau f^2 \Gamma_m E_f E^2}{(1-f)\, E_m^2 R} \right]^{1/3} - \frac{qE}{E_m} \qquad (2)$$

where q is the axial residual stress in the matrix. And finally a lower bound estimate for the maximum stress, based on the statistics of simple fiber bundle failure (failed fibers being assumed to have no load bearing capacity, which is not true), is given by

$$\sigma_U = f\, \hat{S} \exp\left[-\frac{[1-(1-\tau D/R\hat{S})^{m+1}]}{(m+1)[1-(1-\tau D/R\hat{S})^m]} \right] \qquad (3)$$

with

$$(R\hat{S}/\tau D)^{m+1} = (A_O/2\pi RL)\,(RS_O/\tau D)^m\,[1-(1-\tau D/R\hat{S})^m]^{-1} \qquad (4)$$

Here $\hat{S}$ is a strength parameter, S_O the Weibull stress scale parameter, m the Weibull modulus, A_O a scale parameter (usually set equal to 1m^2), and L is the specimen gage length. In order to use Eq. (3), it is necessary to determine $\hat{S}$ by solving Eq. (4) numerically, using experimental values for S_O and m. In the present case, $f = 0.46$, $\Gamma_m \cong 20$* Jm^{-2}, $R = 8\mu\text{m}$, $E_f = 189$ GPa, $E_m = 85$ GPa, $E = 124$ GPa, $q \cong -50$**MPa (negative q are compressive), and L = 8.9 mm. The value of S_O was computed on the basis of[4]

$$A_O S_O^m = 2\pi RLS_1^m/(1n2) \qquad (5)$$

where S_1 is the median in a Weibull fiber strength distribution. Based on Weibull data generated in tensile experiments performed by Prewo[9] using fibers extracted from the ceramed LAS II matrix, m was found to equal 3.1, and S_O was estimated to be 14.2 MPa.

---

* T. J. Clark and J. S. Reed, Am. Ceram. Soc. Bull., 65 [11] 1506-12 (1986).

**D. B. Marshall and A. G. Evans, J. Am. Ceram. Soc., 68 [5] 225-31 (1985).

Based on Eq. (3) and the appropriate physical parameters, it is possible to compute the relationship between τ and D shown in Figure 8. It will be recalled that for two cases, it was possible to measure D, i.e., for $\dot{\varepsilon} = 1.15 \times 10^{-5} s^{-1}$, D $\approx$ 310 μm, and for $\dot{\varepsilon} = 346 s^{-1}$, D $\approx$ 515 μm, which correspond to τ = 2.2 MPa and 1.02 MPa, respectively (Table I). In addition, it is clear that for large D values, τ must approach a very low level. Thus, assuming that D for the two highest strain rates were equal to at least half the specimen gage length, the corresponding value for τ would not exceed 0.038 MPa. These estimates of sliding shear resistance are summarized in Table II.

Also included in the Table are theoretical (Th) and experimental (Exp) values of σ_O (Eq. (2)) and σ_U (Eq. (3)). For the two cases in which periodic cracking was observed, the predicted and measured values of σ_O and σ_U are in reasonable agreement; σ_U^{Th} is expected to be a lower bound, in any case. However, the trend in σ_U with decreasing τ is predicted to be slowly decreasing, while it clearly is rapidly increasing (followed by a mild drop when $\dot{\varepsilon} = 1100 s^{-1}$).

It is obvious that the theoretical model[5] is inconsistent with the physical events attending failure at higher strain rates. In particular, following the nucleation of the dominant matrix crack, fibers begin to slide at such a rate that τ drops precipitously. Until that time, τ must be on the order of 1-2 MPa, and the dominant cracks probably form at a stress level much higher than the predicted 138 MPa.

Table II. Theoretical and Experimental Fracture Parameters

$\dot{\varepsilon}$ (s^{-1})	τ (MPa)	σ_O^{Th} (MPa)	σ_O^{Exp} (MPa)	σ_U^{Th} (MPa)	σ_U^{Exp} (MPa)
1.15×10^{-5}	2.2	303	395	433	585
346	1.02	253	380	429	683
947	0.038	138	---	420	868
1100	0.038	138	---	420	810

Values of τ as low as 0.038 MPa, combined with the observation of globular debris associated with fiber pullout, suggest that the matrix is melting during fiber sliding. This is not as unreasonable as it might seem, given the apparent velocities involved in the pullout process. For the highest strain rate, $1100s^{-1}$, fibers are extracted over a distance of approximately 4.5 mm in about 2 μs. This corresponds to a sliding speed of 2250 m/s, a rate which would probably produce immense frictional heating, even in so short a time.

It is interesting to consider the strength-strain rate dependence for the three dynamic experiments, plotted in Figure 9 (the error bar at $\dot{\varepsilon} = 1100s^{-1}$ signifies the uncertainty discussed earlier in the actual strain rate). Once the strain rate exceeds some critical value, situated between $346s^{-1}$ and $947s^{-1}$, the specimen contains only one major crack. The faces of this crack are bridged by fibers sliding with little resistance within the matrix. Because τ is so low, frictional load transfer is insufficient to load the sliding fibers to the level necessary to sample their Weibull flaw distribution. Only those fiber segments bridging, and extending a short distance below, the main crack interface experience high stresses, and these segments are short -- so short that the fibers must fail at sites other than their weakest links.

Thus, at $\dot{\varepsilon} = 947s^{-1}$, fibers are sliding throughout the specimen, when the stress level near the interface reaches a level sufficient to break a number of the fibers within the sector. The overall stress level drops, as the load is transferred to the remaining "stronger" fibers, causing the load to increase again (the first post-failure peak in Figure 4), a process which is repeated several times until all the fibers have failed in the near-interface region of the main crack. On the other hand, at $\dot{\varepsilon} = 1100s^{-1}$, the sliding shear resistance is sufficiently low that just below the stress level required to fail the most highly stressed fibers, they break free all along the specimen length, creating the first load drop (failure), following which subsequent load transfer and near-interface fiber fracture proceed as described above.

The crucial implication of this scenario is that at still even higher strain rates, the ultimate strength will be even further reduced. Eventually, the strength will approach that required simply to create the first matrix crack. Experiments at higher rates of loading are required in order to test the validity of this hypothesis.

VI. ACKNOWLEDGEMENTS

The authors are grateful for the support of the Office of Naval Research under Contract N00014-83-C-0213.

VII. REFERENCES

1. R. W. Goettler and K. T. Faber, "Interfacial Shear Stresses in Fiber-Reinforced Glasses," 37 129-47 (1989).

2. D. C. Phillips, "Interfacial Bonding and the Toughness of Carbon Fibre Reinforced Glass and Glass-Ceramics," J. Mater. Sci., 9 [11] 1847-54 (1974).

3. A. G. Evans and D. B. Marshall, "The Mechanical Behavior of Ceramic Matrix Composites," Acta Metall., 37 [10] 2567-83 (1989).

4. M. D. Thouless, O. Sbaizero, L. S. Sigl, and A. G. Evans, "Effects of Interface Mechanical Properties on Pullout in a SiC-Fiber-Reinforced Lithium Aluminum Silicate Glass-Ceramic," J. Am. Ceram. Soc., 72 [4] 525-32 (1989).

5. H. C. Cao, E. Bischoff, O. Sbaizero, M. Ruhle, and A. G. Evans, "Effect of Interfaces on the Properties of Fiber-Reinforced Ceramics," J. Am. Ceram. Soc., 73 [6] 1691-99 (1990).

6. D. B. Marshall and W. C. Oliver, "Measurement of Interfacial Mechanical Properties in Fiber-Reinforced Ceramic Composites," J. Am. Ceram. Soc., 70 [8] 542-48 (1987).

7. D. C. Cranmer, "Tribological Properties of Glass Ceramics," Com. Am. Ceram. Soc., 67 [9] C-180-82 (1984).

8. D. B. Marshall, "Interfaces in Ceramic Fiber Composites," pp. 859-68 in Ceramic Microstructures: The Role of Interfaces, Edited bv J. A. Pask and A. G. Evans. Plenum Press, New York, 1988.

9. K. M. Preivo, "Advanced Characterization of SiC Fiber Reinforced Glass-Ceramic Matrix Composites," ONR Interim Report, Contract No. N00014-81-C-0571, June 1983.

10. J. J. Brennan, "Additional Studies of SiC Fiber Reinforced Glass-Ceramic Matrix Composites," ONR Annual Report, Contract No. N00014-82-C-0096, April 1984.

11. T. Nicholas, "Tensile Testing of Materials at High Rates of Strain," Exp. Mech., 21 [5] 177-85 (1981).

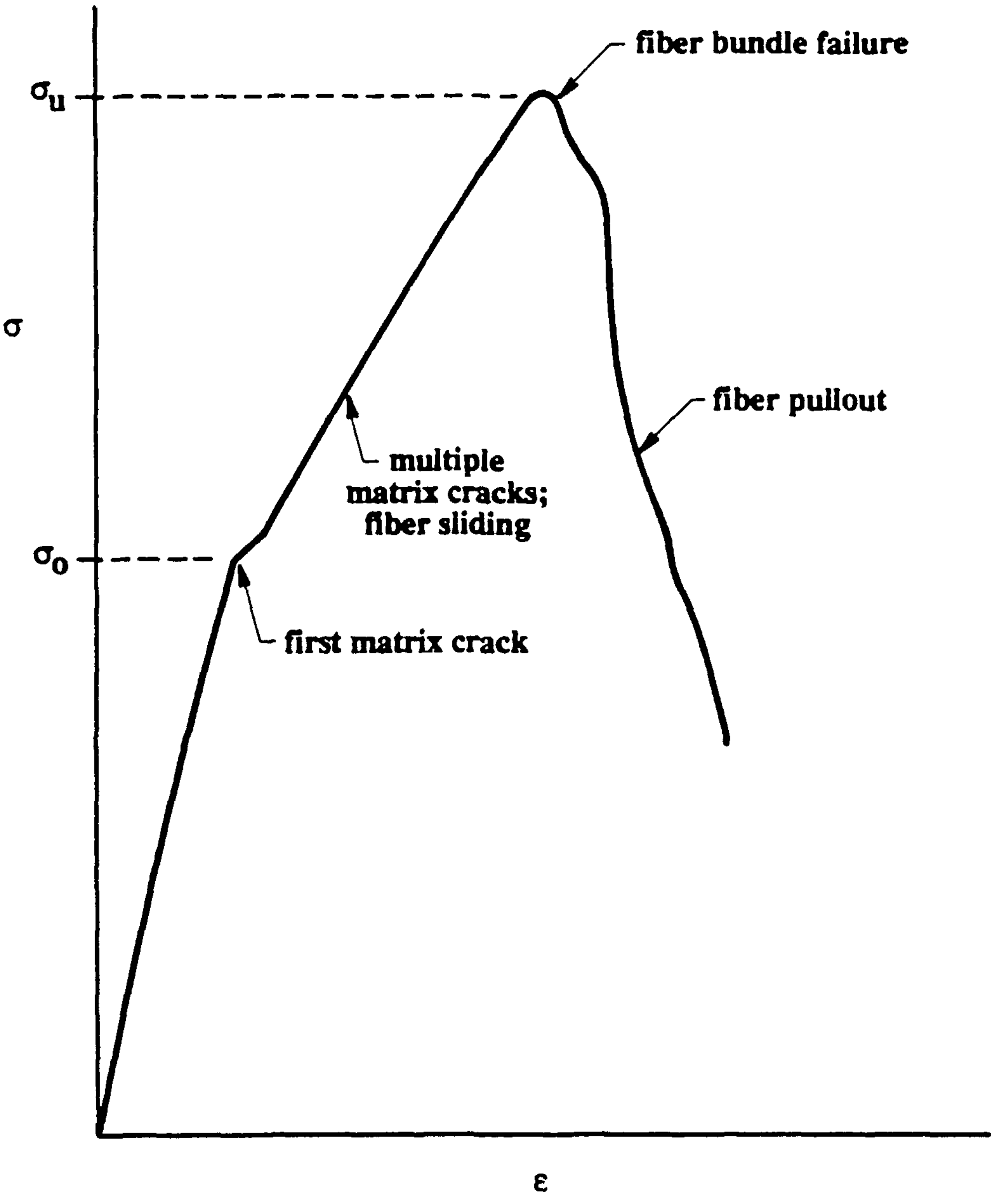

Figure 1. Schematic of fiber-reinforced composite stress-strain response and associated damage processes.

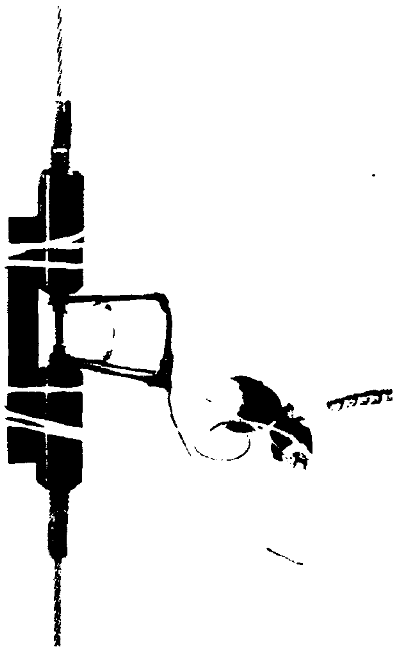

Figure 2. Photo of quasi-static tensile test setup.

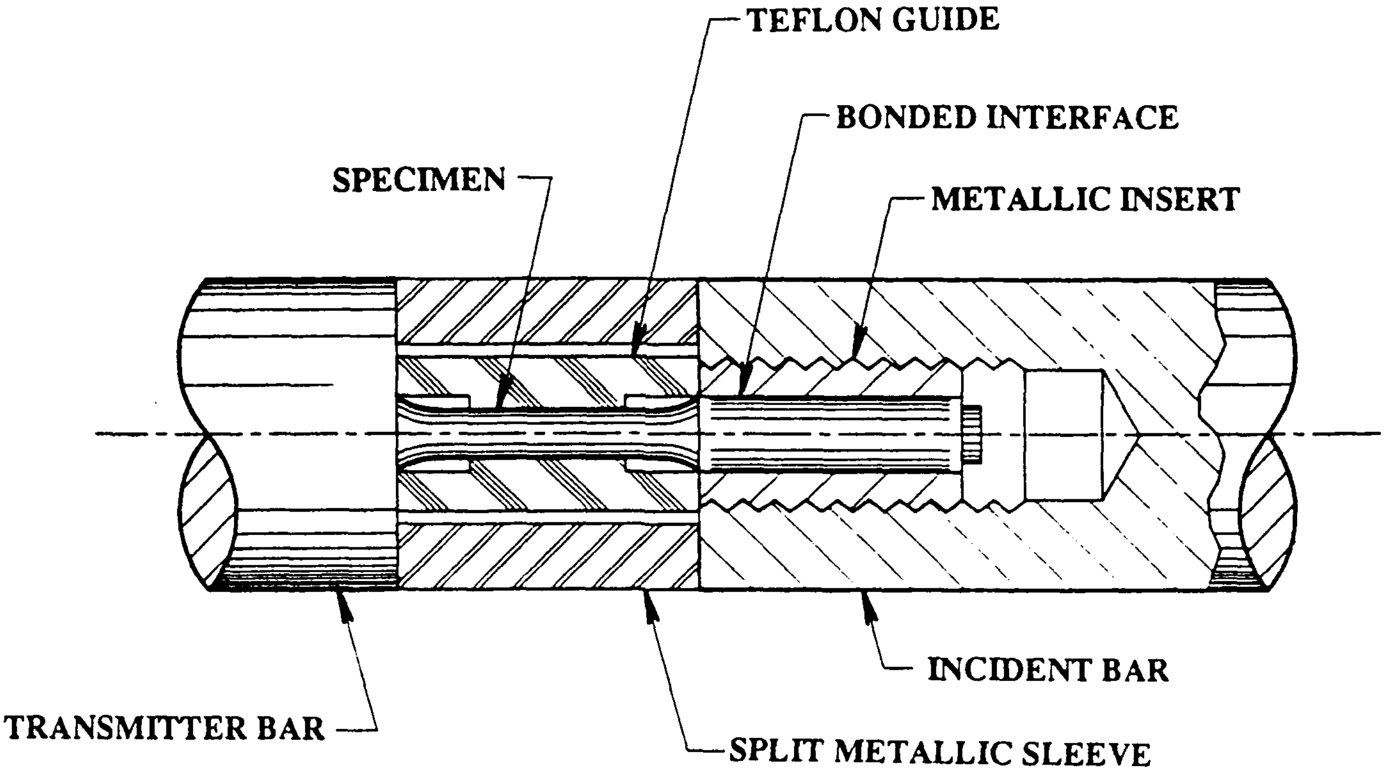
TEFLON GUIDE
BONDED INTERFACE
SPECIMEN
METALLIC INSERT
INCIDENT BAR
TRANSMITTER BAR
SPLIT METALLIC SLEEVE

Figure 3. Schematic of SHPB tensile specimen.

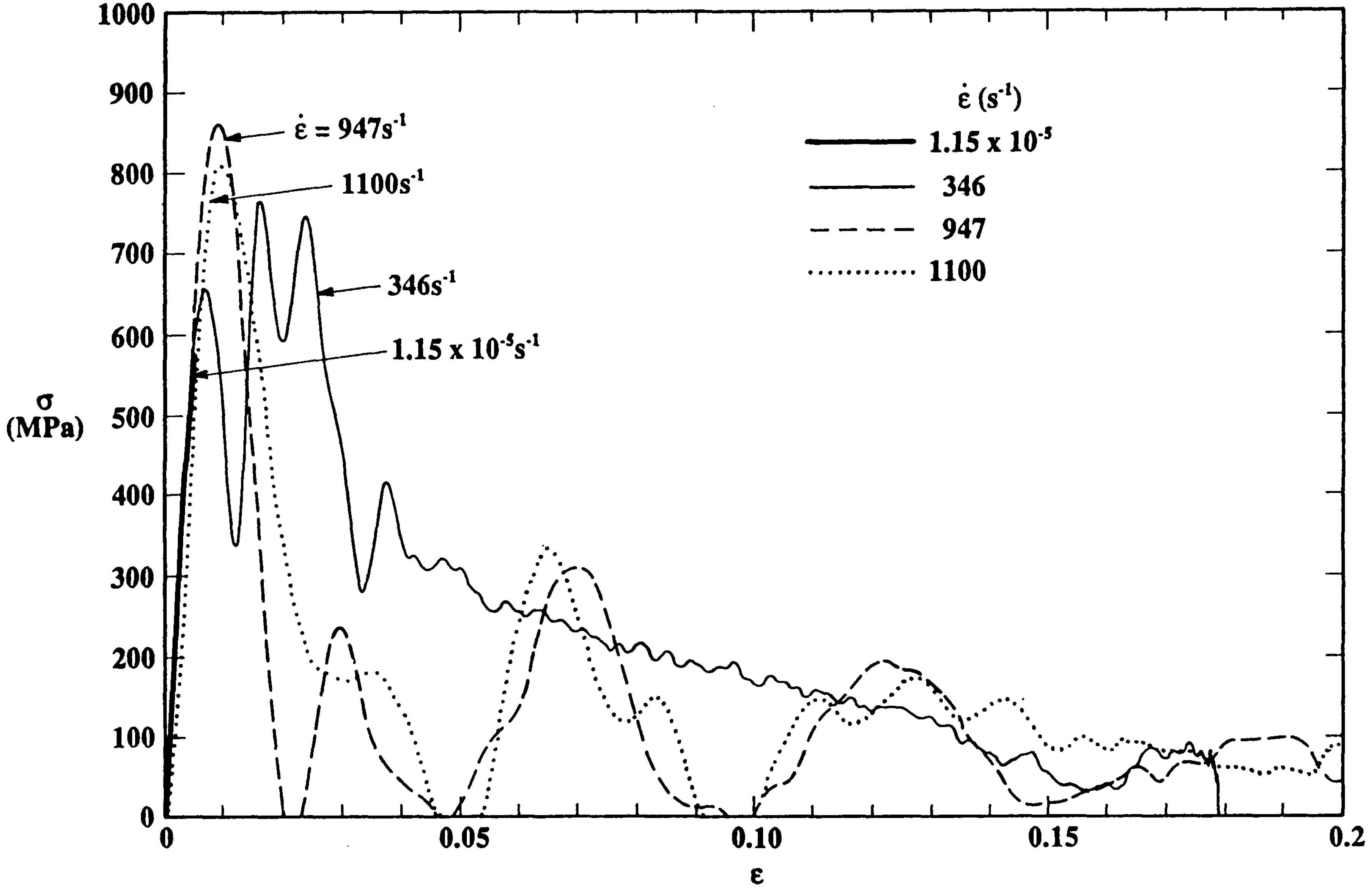

Figure 4. Quasi-static versus dynamic stress-strain response.

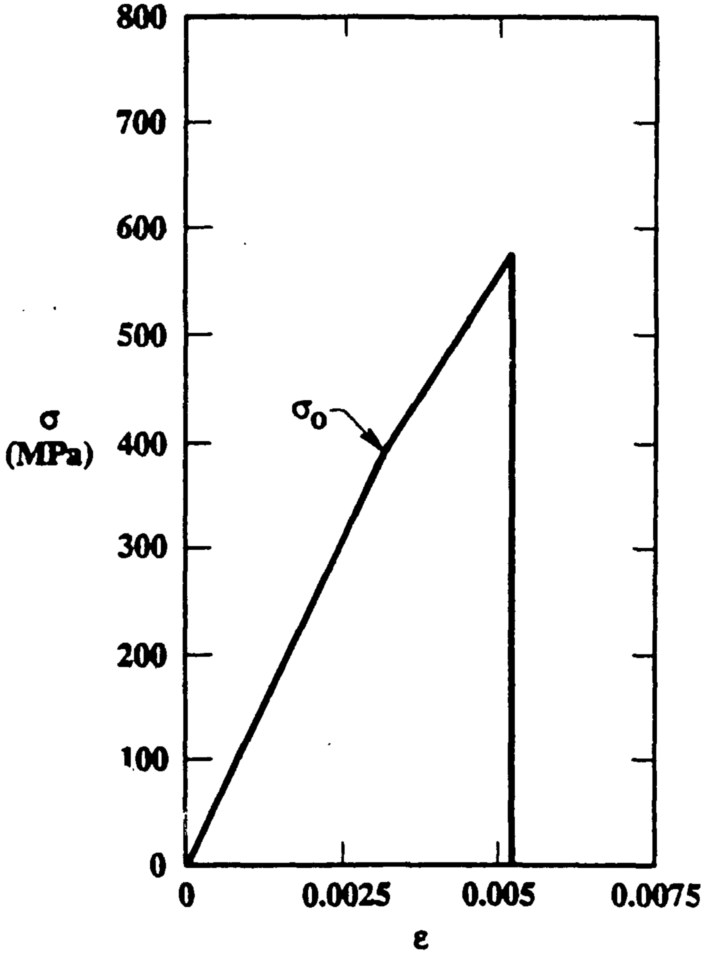

Figure 5(A). Stress-strain details, $\dot{\varepsilon} = 1.15 \times 10^{-5} s^{-1}$, showing inelastic yielding.

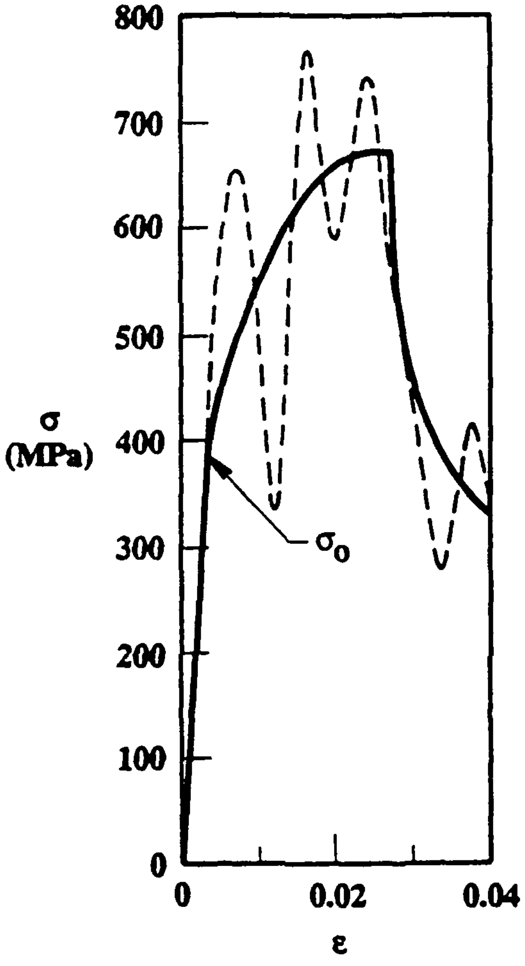

Figure 5(B). Stress-strain details, $\dot{\varepsilon} \approx 346 s^{-1}$, showing extensive non-linear flow prior to failure.

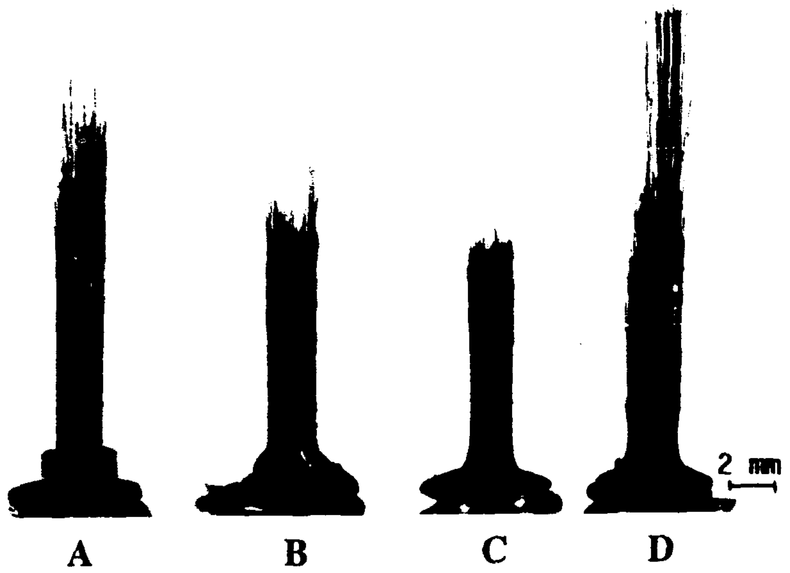

Figure 6. Macroscopic view of specimen failure, showing varying degrees of fiber pullout. (A) $\dot{\varepsilon} = 1.15 \times 10^{-5} s^{-1}$; (B) $\dot{\varepsilon} = 346 s^{-1}$; (C) $\dot{\varepsilon} = 947 s^{-1}$; (D) $\dot{\varepsilon} = 1100 s^{-1}$.

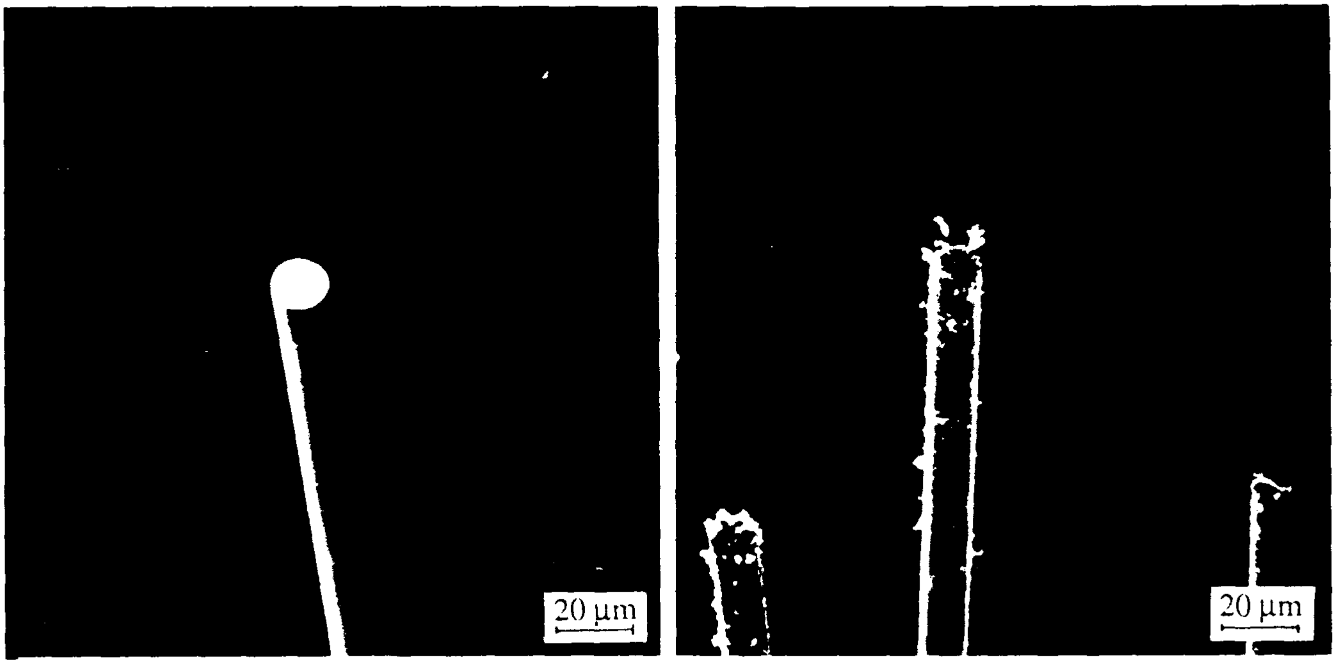

(A) $\dot{\varepsilon} = 1.15 \times 10^{-5} s^{-1}$; clean fibers. (B) $\dot{\varepsilon} = 947 s^{-1}$; debris adhering to fibers.

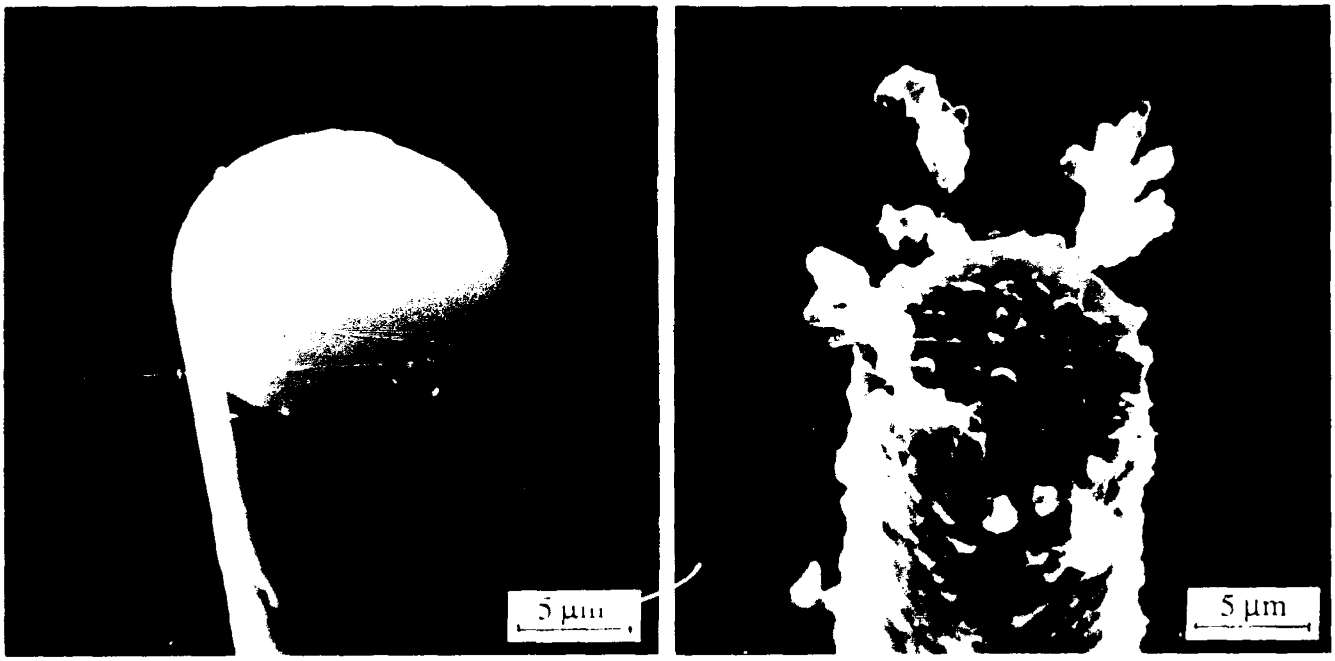

(C) Detail of (A). (D) Detail of (B).

Figure 7. SEM of pulled out fibers.

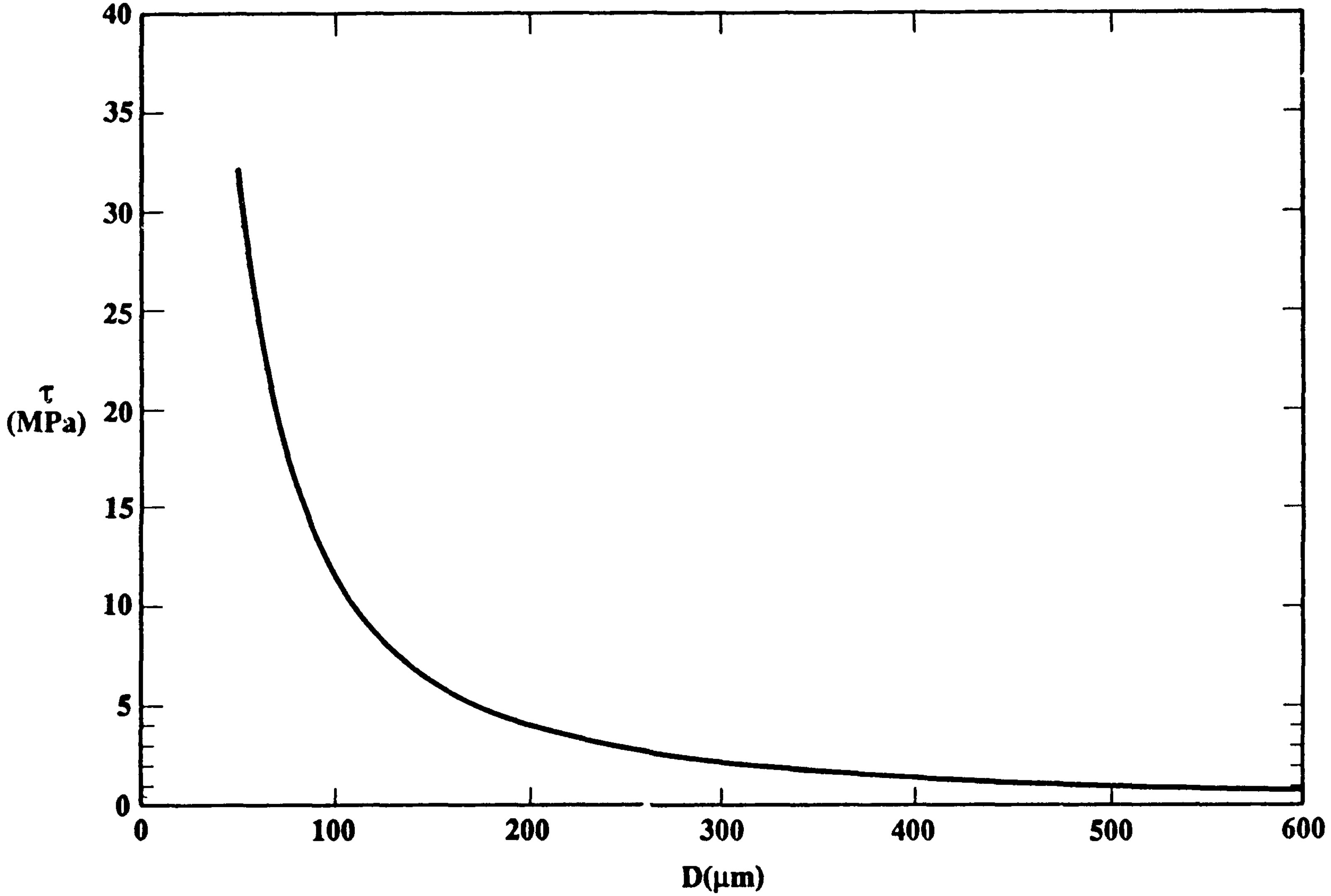

Figure 8. Debonded interfacial shear resistance versus matrix crack spacing.

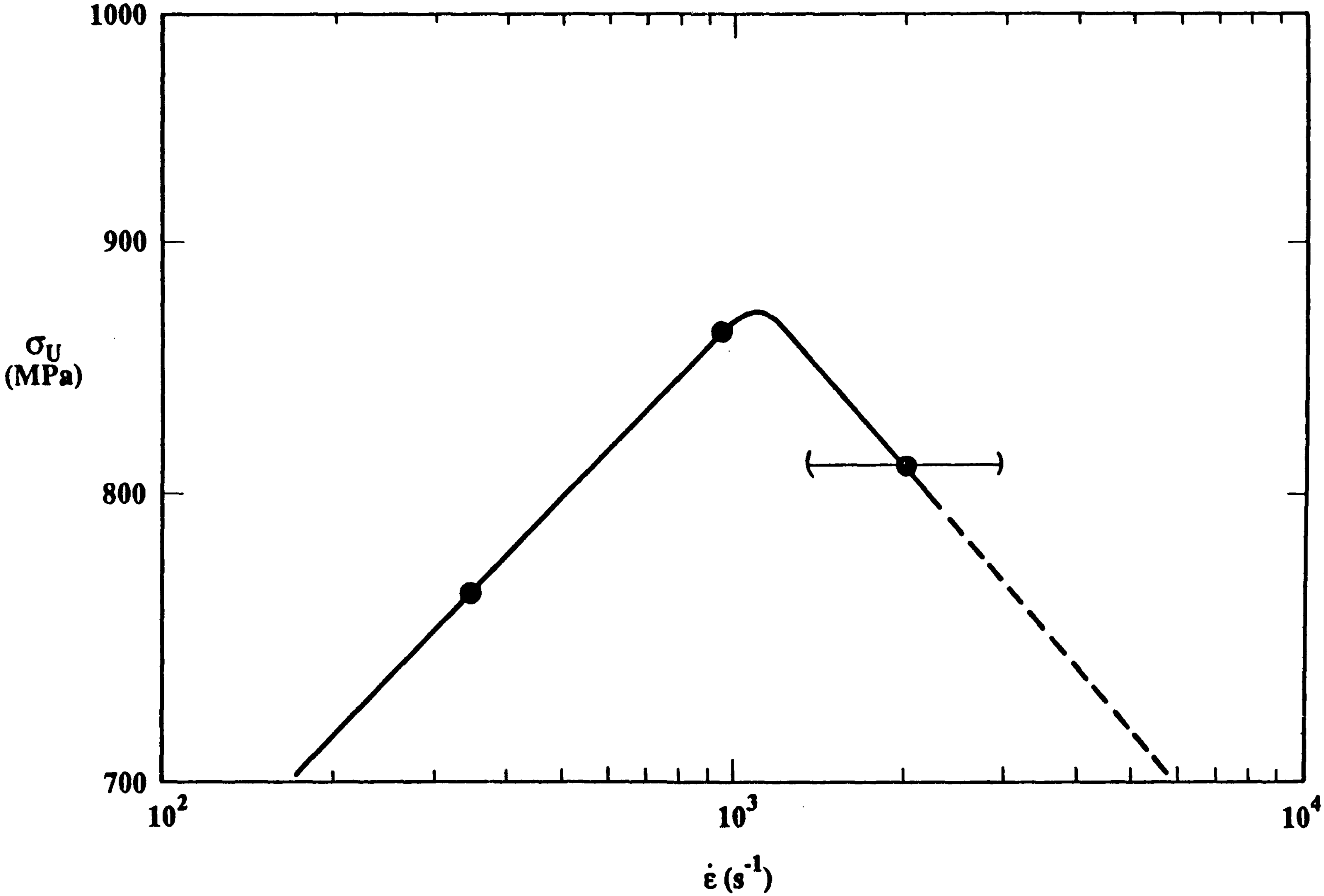

Figure 9. Ultimate strength versus dynamic strain rate.